Interactions of 100 MeV/nucleon ^{40}Ar with Uranium

by

Kenneth Alan Frankel

Abstract

Fragments produced in the interactions of 100 MeV/nucleon ^{40}Ar projectiles with a uranium target have been measured at energies from 10 to 130 MeV/nucleon at angles from 10° to 170°. Nuclei with charge $5 \leq Z \leq 10$ were observed.

The data can roughly be divided into two groups, corresponding to central and peripheral collisions. The central collision data can be fit with a thermal model that uses two recoiling sources. The source velocities are consistent with the predictions of the fireball and target explosion models, but the source temperatures inferred from the data are higher than one would expect on the basis of energy and momentum conservation. These results are similar to those obtained in previous studies at beam energies of 400 and 500 MeV/nucleon. The data also follow the pattern of the universal curve of invariant cross section vs momentum observed at higher beam energies by Price et al. The projectile fragmentation data are also fit by two thermal sources. There are indications that the observed temperatures are higher than one would expect on the basis of other projectile fragmentation studies.

The projectile fragmentation data are studied in terms of a simple friction model. Order of magnitude estimates show that the data may be consistent with the model, but further development, calculation and experimentation are necessary to check the validity of the model at this beam energy.

A preliminary investigation is made of the possibility that the projectile may pick up one or more target nucleons before it fragments. This process leads to widening of the distributions at large momentum transfers.

From this broad survey we find that much of the spectrum can be described by falling exponentials in energy in the emitting frames. We conclude that the observed spectrum is due to nonthermal sources as the temperatures derived from the slopes of the exponentials are greater than those we predict.

Acknowledgments

I would like to thank Professor P. B. Price for his advice and encouragement. Other members of the Price group who provided assistance and advice include John Stevenson, Ed Shirk, Mike Solarz and Greg Tarlé.

Colleen Dunlavy and John Stevenson deserve special thanks for the many hours they spent measuring tracks.

I am thankful to Fred Lothrop and the staff at the Lawrence Berkeley Laboratory Bevalac for providing the ^{40}Ar beam.

I would like to thank Judy Blair for typing my thesis. Her skill and advice were an invaluable aid.

Thanks go to countless friends who gave me encouragement through the years.

Finally, I would like to thank the U.S. Department of Energy for providing financial support of the work described in this thesis.

Table of Contents

Table of Contents (cont.)

Introduction

Many experiments have been conducted recently to study fragments emitted in relativistic heavy ion collisions.[1] These studies have typically been conducted with projectiles up to mass 56 and energies in the range 250 MeV/nucleon to 2100 MeV/nucleon. The most copiously produced charged fragments emitted in these collisions are protons, but fragments with mass and charge greater than unity are quite often seen.

By measuring the distribution of fragments emitted in high-energy nucleus-nucleus collisions we hope to learn about the properties of nuclear matter at greater than normal density and temperature. Heavy ion collisions may provide evidence for nuclear shock waves, density isomers, and Lee-Wick matter.[2] Numerous models have been developed which attempt to explain the distributions of the emitted fragments. Single-particle inclusive cross sections of emitted protons have been qualitatively explained by a number of models, such as nucleus-nucleus cascade,[3,4,5] firestreak,[6] and nuclear hydrodynamics.[7] These models do not require the existence of exotic phenomena, such as shock waves, to explain the data. Because inclusive measurements average over impact parameter, do not take multiplicity effects into account and may result from a number of processes, the effects of compression or new phenomena may not be seen. Experiments to measure pion and cluster emission ($A_{fragment} > 1$) and to measure spectra of emitted fragments as a function of multiplicity have been conducted in the hope that some signature of compression or other new phenomena might be seen. In this paper we will primarily be concerned with the study of emission of fragments of medium mass, especially $8 \leq A_{fragment} \leq 20$.

High-energy heavy ion collisions have generally been divided into two categories: peripheral collisions, where the colliding nuclei barely graze each other, and central collisions, where there is a large overlap of the colliding nuclei. The peripheral collisions have been understood either as a fast process, where each nucleus splits into two pieces "immediately" after colliding, or as a slow process, where the nuclei fragment only after thermal equilibrium has been attained.[8] Central collisions can be quite violent; many fragments of various sizes can be emitted in a single collision. The mechanism for cluster emission is not well understood. For $2 < A_{fragment} \lesssim 6$, the thermodynamic[9] and coalescence models[10] have had some success in explaining the distributions, but they do not work well for heavier fragments.[11] The heavier fragments appear to be emitted from a moving thermal source with a velocity and temperature that is inconsistent with energy and momentum conservation. The data for these fragments exhibit an abnormally high temperature. The origin of the phenomenon is not understood but it is suspected that the fragments are emitted prior to the attainment of thermal equilibrium, where the requirement $E = 3/2\ T\ (k = 1)$ need not be satisfied. Another possibility involves the conversion of random motion to radial motion during decompression. The data from a number of experiments appear to lie on a single universal curve when the invariant cross section in the moving frame of the emitting source is plotted as a function of total momentum.[12] The origin of this curve is unknown. Some underlying physics may explain it or it may be an accident.

We hope that further experimentation may lead to an understanding of how fragments are produced in heavy ion collisions. In this paper

we present results from the experiment 100 MeV/nucleon ^{40}Argon + Uranium → Fragments ($5 \leq Z_{fragment} \leq 10$). Angle and energy distributions are measured at angles from 10 to 170 degrees and from energies of approximately 10 to 130 MeV/nucleon. By working with a 100 MeV/nucleon beam we can measure fragments through a large rapidity region. Fragments can be observed from both central and peripheral collisions in a single experiment. As 100 MeV/nucleon is a basically unexplored region, we can conduct a survey over a large dynamic range to look for unexpected phenomena and to test the models used at higher energies.

From the measurements to be described below, we find that the cross sections fall steeply with increasing fragment energy at most energies and angles. At 10° there is a projectile fragmentation peak at the beam velocity. At small angles and at rapidities between the target and the beam, the cross sections are either flat or fall slowly.

The data, apart from some points in the forward direction, appear to be due to central collisions and are fit reasonably well by a model based on the assumption of thermodynamic equilibrium of two sources. One source has a velocity corresponding to the recoil velocity of a system formed when the projectile and target unite to form a single entity. The second source is the "fireball" source which is formed from the overlap of the nuclear matter of the projectile and target. The overlapping nuclei recoil as a single unit while the nonoverlapping piece of the projectile proceeds near the beam velocity and the corresponding target piece remains near zero velocity. The observed temperatures are much higher than energy and momentum conservation would predict. This situation is similar to that observed at higher energies. A simple fireball model is tried but its

predictions do not fit the data. The data are shown to be consistent with the universal curve of invariant cross section vs momentum, discovered by Price et al.[1,2] The data at very forward angles which we associate with projectile fragmentation are fit by two thermal sources. One source moves at about the beam velocity and has a higher temperature than is normally seen in projectile fragmentation studies. The second source has a velocity of $\beta = \frac{v}{c} \sim -0.1$ in the projectile frame. This source may only be an artifact of the parametrization as it overestimates the data at larger angles.

A friction model of projectile fragmentation has also been studied. While some of the results of the model do not apply to this experiment, we learn that a beam energy of 100 MeV/nucleon may be useful in studying friction phenomena.

In the case of projectile fragmentation with a Gaussian distribution in momentum, the data are symmetric about zero momentum in the frame of the moving source. The data in this experiment are much steeper on the high momentum side of the projectile fragmentation peak than on the lower side. Preliminary studies are made using a simple model that may account for this phenomenon.

From this experiment we learn that the unexplained phenomena observed at higher beam energies, such as high source temperatures and the universal curve in momentum, are also apparent at 100 MeV/nucleon. This experiment covers a much wider dynamic range of cross section, angle and energy than similar experiments at higher energies. Thus, there is increasing evidence that the data for cluster emission are illustrative of significant phenomena in high-energy heavy ion collisions.

Summary of Previous Data and Models

There are a number of experiment and interpretive models that have guided the development of the field of high-energy heavy ion collisions. Here we discuss primarily those experiments and models that have relevance to the subject of this paper.

It is often convenient to divide heavy ion collisions into classes based on impact parameter. At large impact parameter only a small portion of each nucleus is involved in a collision. This is generally referred to as projectile fragmentation or target fragmentation, depending on whether we are looking at particles emitted from the projectile or the target. In these interactions there is little energy and momentum transfer between the target and projectile. At small impact parameters many nucleons are involved in a collision. There is often a large amount of energy and momentum transfer. We should remember that since the impact parameter is a continuous variable, there cannot be a definite separation between interaction regions. When analyzing data we often find that geometrical factors play a major role in our ability to divide collisions into various classes.

1. Central Collisions

Let us first consider collisions with small impact parameter. There is a high multiplicity of fragments. They are often produced at large angles and at velocities between zero and the beam velocity. There is a good deal of overlap of the nuclei. When the projectile is smaller than the target it may be totally enveloped by the target. These interactions are commonly referred to as central collisions.

We can study central collisions by observing proton spectra, fragment spectra of composites (A > 1), or pion spectra. Let us assume the energy is low enough so that pion production is negligible. When building a model for the proton spectrum, it is convenient to fit the model to what I call the primordial spectrum. This is the spectrum that would be observed if composite nuclei were not formed. We define the primordial spectrum to be given by the expression:

$$\left(\frac{d^2\sigma}{d\Omega dE}\right)_{\text{primordial}} = \sum_{\text{all isotopes}} Z \frac{d^2\sigma(Z,A)}{d\Omega dE} \qquad (1)$$

where E is the energy/nucleon.

A. Single Nucleon Emission

The Monte Carlo method can be used to fit the primordial proton spectrum. J. Stevenson has obtained good fits for the reactions 250 and 400 MeV/nucleon ^{20}Ne + U, 400 MeV/nucleon ^{4}He + U, and 800 MeV/nucleon ^{20}Ne + NaF.[3] In this calculation a relativistic nucleus-nucleus collision is treated as a succession of two-body nucleon-nucleon collisions. The model has no free parameters. Each nucleus is taken to be a Fermi gas and the Pauli Exclusion Principle is taken into account for each nucleon-nucleon collision. The model can be used as an aid in the design and analysis of experiments that study central collisions.

The nuclear fireball[13] and firestreak[6] models have also been used to try to explain the proton data. These models involve the geometry of the collision and equilibrium thermodynamics. The fireball model divides the nucleons into participants and spectators. The colliding nuclei are assumed to make clean cuts

through each other. The participants, which contribute to the intermediate energy protons, are the nucleons from the overlapping cylindrical cuts. Conservation of energy and momentum give the velocity and temperature of the resulting fireball.[14] The fireball velocity is given by:

$$\beta = \frac{P_{lab}}{E_{lab}} = \frac{N_p[t(t+2m_{NB})]^{\frac{1}{2}}}{(N_p+N_t)m_{NB}+N_p t} \tag{2}$$

where P_{lab} is the fireball momentum in the lab frame, E_{lab} is the total energy in the lab, t is the projectile incident kinetic energy per nucleon in the lab, m_{NB} is the mass of a bound nucleon (931 MeV), N_p is the number of projectile participants and N_t is the number of target participants.

The center of mass (relativistic) energy is given by:

$$E = [E_{lab}^2 - P_{lab}^2]^{\frac{1}{2}} = [(N_p+N_t)^2 m_{NB}^2 + 2m_{NB}N_p N_t t]^{\frac{1}{2}} \tag{3}$$

The temperature, T, is given nonrelativistically by:

$$T = \frac{2}{3}\left[\frac{E}{N_t+N_p} - m_N\right] \tag{4}$$

where m_N is the mass of a free nucleon (939 MeV).

The fireball, according to this model, then decays with a Maxwellian distribution. Upon integrating over impact parameters one obtains the calculated cross section for protons. The spectators reside in the material in the projectile and target that is not in the overlap region. They decay in their own frames, giving off low-energy fragments.

If the projectile does not make clean cuts, there may be some critical impact parameter for which the fireball does not

escape the target nucleus. This is called "target explosion." One can again use energy and momentum conservation to calculate the expected cross sections. It has been pointed out that this mechanism could be responsible for the 10 to 90 MeV protons produced in 400 MeV/nucleon ^{20}Ne on U collisions.[13]

The firestreak model[6] is similar to the fireball model. The participant projectile and target nuclei are divided into collinear bands. Each band of the projectile interacts only with the corresponding target band in front of it. There is no communication between bands. This method is useful because it conserves angular momentum. The model also makes use of a diffuse nuclear surface. These improvements over the fireball model enable the firestreak model to fit the data better than the fireball model.[6]

B. Composite Fragments

The study of cluster emission has proven to be an interesting problem. Two models that have been used to describe the emission of light fragments are the coalescence model of Gutbrod et al.[10] and Mekjian's statistical thermodynamic model.[9] In the coalescence model a fragment can be formed when there are A nucleons within a momentum sphere of radius p_o. The cross section for production of the fragment is proportional to the Ath power of the single nucleon cross section. This model was shown to fit ^{20}Ne + U reactions at 250 MeV/nucleon and 400 MeV/nucleon for ^{2}H, ^{3}H, ^{3}He, and ^{4}He, given the spectrum of ^{1}H. Mekjian applies thermodynamics to obtain the cross sections for composite nuclei and he derives the connection between his model and the coalescence model. He obtains his cross sections as a function

of impact parameter.

For fragments of charge greater than two it is convenient to fit the data to models with three or more parameters. If we are using a thermodynamic model we may choose:

$$\frac{d^2\sigma}{d\Omega dE} = K\sqrt{E}\, e^{-E/\tau} \qquad (5)$$

to be the nonrelativistic cross section in the frame of a moving source. The parameters are K, β, and τ. K gives the overall normalization. τ is often taken to be equal to, or a simple function of the source temperature, and β is the velocity of the source. From the fitted β and τ we can attempt to explain the physics of the reaction. For example, if a fragment were emitted from an infinitely massive source in thermal equilibrium, τ would be the temperature of the source. We should note that the parameters do not refer to a single discrete source, but to an average over a continuum of sources.

Let us consider the reaction 400 MeV/nucleon $^{20}Ne + U \rightarrow B +$ anything. For 10 MeV/nucleon $\leq E_{fragment} \leq$ 40 MeV/nucleon Gosset et al.[14] parametrize their data by $\beta = 0.06$ and $\tau = 27$ MeV. The center of mass velocity of the projectile-target system is $\beta = 0.08$ and the target explosion temperature for a gas of nucleons is 13.5 MeV. The authors claim that the source velocity could mean that these fragments are preferentially emitted by the most central collisions. The system formed then decays by a thermal equilibrium mechanism. The authors say the higher temperature is in the correct direction when composite particles are taken into account in the fireball. For the same reaction in a different

experiment Stevenson et al.[9] found for 30 MeV/nucleon $\leq E_{fragment} \leq$ 50 MeV/nucleon that the recoiling source could be fit with a velocity β of 0.091 and τ = 62 MeV. They claim this is evidence for the production of slowly moving, highly excited nuclear matter. The β and high τ are inconsistent with energy and momentum conservation if τ is taken to be the source temperature. This suggests that the slow source is nonthermal as the internal energy need not be 3/2 τ per nucleon. Ta Cheung[15] has analyzed several reactions and he claims to be able to account for the low velocity (but not the high τ) of the slow source based on the kinematics of the collisions.

We can also parametrize the slow source by an exponential in momentum. Price et al.[12] have analyzed a number of experiments and have shown that the invariant cross sections of all fragments appear to define a universal curve that is exponential in momentum. They evaluate the momentum in a frame in which the distribution is isotropic. The reason for the existence of the curve is unknown. The authors suggest further experimentation over a wide range of fragment mass and momentum as a test of the curve's applicability.

2. Peripheral Collisions

Let us next consider projectile fragmentation. Greiner et al.[16] have observed projectile frame fragments with the 0-degree spectrometer at the Bevalac. They measure fragment momentum distributions that are Gaussian in shape, with small momentum transfer to the projectile nucleus. The fragments are typically measured to a total momentum of 400 MeV/c in the projectile frame. The widths of the

Gaussian can be given by:

$$\sigma^2 = \sigma_o^2 \frac{K(A-K)}{A-1} \tag{6}$$

where K is the fragment mass, A is the projectile mass, and σ_o is a constant, approximately 90 MeV/c.[8]

Goldhaber[8] has shown that projectile fragmentation is consistent with the sudden liberation of virtual clusters or with the attainment of thermal equilibrium. In the sudden model Goldhaber calculates the mean square momentum $\langle p_k^2 \rangle$ of k nucleons chosen at random from a box of A nucleons with mean square momentum $\langle p^2 \rangle$. Using conservation of momentum, it is a simple exercise in combinatorics to show:

$$\langle p_k^2 \rangle = \frac{K(A-K)}{A-1} \langle p^2 \rangle \tag{7}$$

with $\langle p^2 \rangle$ = 3/5 of the square of the Fermi momentum. One can extend this calculation by computing higher moments. These moments could be checked with the higher moments of the Gaussian distribution. This could tell us if we expect fragments with momenta much greater than the Fermi momentum still to be characterized by a Gaussian distribution.

Goldhaber showed that if the projectile nucleus comes to thermal equilibrium and divides into two fragments, then σ is related to the temperature by:

$$\sigma^2 = m_N T \frac{K(A-K)}{A} \tag{8}$$

where the temperature T corresponds to about 9 MeV and m_N is the nucleon mass. He also notes that if there is some momentum transfer to the projectile nucleus, then there will be an increase in the width of the distribution. This is given by:

$$\sigma'^2 = \sigma^2 + P_i^2 (K/A)^2 \tag{9}$$

for mean squared momentum p_i^2 in the i direction.

Feshbach and Huang[17] have also examined projectile fragmentation. If we take their results and apply them to the case where the projectile splits into two equal size fragments, then we essentially reproduce Goldhaber's results for the widths of the Gaussians. The results show that, in the approximation that the fragment momentum is below the Fermi momentum, we expect a Gaussian distribution.

Goldhaber's and Feshbach and Huang's results do not rule out mechanisms different from the ones they discussed when we look at high momentum fragments. These fragments may come from a projectile that has undergone large momentum transfer. It may be possible to derive the distributions based on Feshbach and Huang's model but the computations are difficult. J. Stevenson[18] have performed a Monte Carlo calculation for a mass 3 fragment emitted from an infinite mass nucleus. Using a σ = 387 MeV/c and a Fermi momentum of 250 MeV/c he finds the deviation from a Gaussian to be less than 30% to a momentum of 1300 MeV/c. The discrepancy greatly increases at larger momenta. Effects of a finite projectile nucleus and momentum transfer will alter these results, but they suggest the possibility of seeing the Gaussian distribution out to rather large momenta.

Westfall et al.[19] have observed the target frame analogue of projectile fragmentation. They measured energy spectra of fragments produced with 2.1 and 4.9 GeV proton beams. They used both light (C and Al) and heavy (Ag and U) targets. They fit their data to a Maxwell-Boltzmann distribution that incorporated two-body breakup kinematics and a Coulomb barrier with smearing. The distribution in the moving frame is:

$$\frac{d^2\sigma}{dE^*d\Omega^*} = \frac{\sigma_i}{2(\pi\tau_i)^{3/2}} \sqrt{E^*}\, e^{-E^*/\tau_i} \qquad (10)$$

where E^* is the kinetic energy available in the two-body breakup, σ_i is the total cross section for ith fragment and τ_i is the temperature. They find the data can be fit by the sum of two distributions. For light targets the emitting system can be characterized by $\beta_1 = 0.005$, $\tau_1 \sim 7$ MeV, $\beta_2 \sim 0.01$, and $\tau_2 \sim 13$ MeV. For the heavy targets they find $\beta_2 \sim 0.006$ and $\tau_2 \sim 15$ MeV. They interpret the low temperature component to be the result of the sudden breakup of a nucleus involved in a peripheral collision. The high temperature component is interpreted as being the result of a central collision where there has been a high deposition of energy in the emitting nucleus. The transition to the high energy component occurs at approximately an energy of 10 MeV (or a total momentum ~360 MeV/c) at 90° for ^{7}Be emitted from p + C reactions. It is not too difficult to see the high energy component if we can observe fragments with several hundreds of MeV of kinetic energy.

The distribution of $p_{\parallel}$ in projectile fragmentation is approximately a Gaussian with a peak at a momentum $\sim -10^2$ MeV/c in the projectile frame. This slow-down of the projectile has been analyzed as a friction phenomenon by Abul-Magd et al.[20] They develop a simple model that predicts the average parallel momentum transfer to the fragment.

The interaction is studied in the rest frame of the projectile. Suppose that one projectile nucleon received a momentum transfer $\vec{q}$ from the target. The nucleon may escape the potential well, -U, with momentum $\vec{q}'$ if

$$\vec{q}^2/2m - U = \vec{q}'^2/2m > 0 \tag{11}$$

where m is the nucleon mass.

By momentum conservation the momentum of the fragment is given by $\vec{P} = \vec{q} - \vec{q}'$. The momentum gain of the fragment is described by a friction coefficient f, so that:

$$\vec{p} = f\vec{q} \tag{12}$$

where isotropy is assumed ($\vec{q}'$ parallel to $\vec{q}$). Solving for f gives:

$$f = \frac{2mU}{\vec{q}^2+\vec{q}\cdot\vec{q}'} \approx \frac{1}{2}\frac{U}{\vec{q}^2/2m} \tag{13}$$

This gives $f \approx 1/3$ for $U \approx 50$ MeV and $\vec{q}^2/2m \approx 80$ MeV.

The next step is to determine $\langle P_{\parallel} \rangle$, the average fragment momentum component in the beam direction. Let $\vec{\pi}_o$ be the projectile momentum. Energy conservation gives:

$$(m^2+\vec{\pi}_o^{\,2})^{\frac{1}{2}} = (m^2+(\vec{\pi}_o-\vec{q})\,)^{\frac{1}{2}} = \vec{q}^2/2m \tag{14}$$

Using as a simple approximation $\vec{\pi}_o \cdot \vec{q} = -\pi_o q_{\parallel}$ we have:

$$q_{\parallel} = -\vec{q}^2/2m\ (1+\eta(\tfrac{m}{\pi_o})); \quad \eta(x) = x + \frac{1}{2}x^2 + \ldots \tag{15}$$

Thus Abul-Magd et al. obtain

$$\langle p_{\parallel} \rangle = -\frac{1}{2}(1+\eta(\tfrac{m}{\pi_o}))\ \langle U \rangle \tag{16}$$

At 2 GeV/nucleon $\eta = 0.4$. A typical value of $\langle U \rangle$ is given as $\langle U \rangle \leq 50$ MeV. For an ^{16}O projectile and a ^{15}N fragment the model predicts that $\langle P_{\parallel} \rangle$ is negative and $|\langle P_{\parallel} \rangle| \leq 35$ MeV/c, while experiment gives $\langle P_{\parallel} \rangle = -21$ MeV/c.

The model can be further refined by taking into account the effects of Fermi motion, the $\vec{r}$ dependence of the potential, and $\vec{P}$ not necessarily being parallel to $\vec{q}$. The authors develop a classical model which assumes that a nucleon of mass m orbits a nuclear core of mass M. The reduced mass of the system is given by $\frac{1}{\mu} = \frac{1}{m} + \frac{1}{M}$. Solving the energy and momentum conservation equations gives:

$$\langle P_{\parallel} \rangle = -\frac{1}{2}\left(1+\eta\left(\frac{m}{\pi_o}\right)\right) \cdot \left(\left\langle \frac{P^2(+\infty)}{2\mu} \right\rangle + E_B\right) \qquad (17)$$

where E_B is the binding energy of the knocked out nucleon, and $\langle P^2(+\infty) \rangle = 3\sigma_{\parallel}^2$, the longitudinal momentum width. For multi-nucleon removal the nucleons are assumed to be kicked out one after another and then the contributions to $\langle P_{\parallel} \rangle$ are summed. $\langle P^2(+\infty) \rangle$ and E_B refer to a situation where the projectile and fragment differ by several nucleons.

The model works very well for removal of 1 or 2 nucleons from the projectile. Since the projectile is often left in an excited state after a collision, it may lose energy by emission of nucleons or heavier fragments. The process where nucleons are struck from the projectile is referred to as abrasion, while the decay of the excited projectile nucleus is called ablation. A full abrasion-ablation calculation is necessary to account for multi-nucleon removal. This calculation predicts $\langle P_{\parallel} \rangle$ quite well for 2 GeV ^{16}O fragmentation to mass 15 through mass 12.

3. Exotic Phenomena

Some recent experiments have shown that compression and shock wave phenomena may occur in high energy heavy ion collisions. P.J. Siemens and J.O. Rasmussen presented evidence for a blast wave

in collisions of 800 MeV/nucleon Ne on NaF.[21] From analysis of cross sections for emitted protons and pions, they claim that in the center of mass frame there is a peaking in the velocity distribution about the mean radial expansion velocity and that there is a reduction of intrinsic excitation due to cooling which accompanies the expansion. As the system contains only 40 nucleons, it is difficult to see how such a system could generate a shock wave. Further experimentation and theoretical analysis should lead to more knowledge about these possible shock waves.

Wolf et al. have measured the pion spectra in the reaction 1.05 GeV/nucleon $^{40}Ar + {}^{40}Ca \rightarrow \pi^+ + X$.[22] They find that the π^+ mid-rapidity distribution is anomalous relative to proton-proton, to proton-nucleus, and to many heavy ion reactions. They find that both cascade and thermal models fail to explain the data. They suggest that the measured distribution may be a signature of processes which occur in the early stages of a heavy ion reaction, such as compression. A model that incorporates compression and makes a reasonable fit to the data is necessary before the evidence will be convincing.

4. Proposal

We see that measurements have been made over a large kinematic region. The relationships between these results and their correspondence to theory are often difficult to determine. We would like to know as much as possible what happens in a single relativistic heavy ion collision. It would be useful to look at heavy fragments through the entire kinematic range, from near zero velocity to beam velocity and beyond. Such a broad-band experiment has been conducted for proton emission and has given insight into the applicability of

various models such as the firestreak model.[23] A broad-band experiment to measure heavy fragments could test various models of composite formation and show where the regions of their applicability exist.

Let us consider what we might expect to see with a 100 MeV/nucleon beam. This is a convenient energy as we only need 3 cm of Lexan plastic detector to stop a ^{11}B with the beam velocity. At forward angles we should see the projectile and target contributions as well as the intermediate rapidity region in between. At larger angles the typical exponential decays should appear.

There are some drawbacks to working at 100 MeV/nucleon. Until recently the Bevalac could not operate at energies below 250 MeV/nucleon, so the energy region around 100 MeV/nucleon has not been explored. At 250 MeV/nucleon $\beta = 0.62$ while for 100 MeV/nucleon $\beta = 0.43$. At 100 MeV/nucleon the velocity is still reasonably high so we may still be able to test models that apply at higher energies. The energy deposition will be smaller, but the beam energy is much higher than the nuclear binding energy. As 100 MeV/nucleon is still a basically unexamined region, it may contain interesting physics of its own. The proton-proton cross section begins to rise at 100 MeV and we may also be experimenting near the nuclear sound velocity.

For our apparatus the smallest angle we look at is 10°. This limits the minimum detectable momentum of a fragment in the projectile frame to $p_{min} \simeq Km_N V_{beam} \sin 10°$ (K is the fragment mass in amu) in the nonrelativistic approximation. For K equal 12 this is 800 MeV/c. At 10° it is quite likely that we may miss the fragmentation of the type seen by Greiner et al., unless the Gaussian shape of the momentum distribution holds out to several σ.

Interactions of ^{16}O nuclei with nuclei in nuclear emulsions have recently been studied by Kullberg et al.[24] They claim that the parallel momentum distributions show emission of fragments from systems with mean velocities of $\beta = 0.06$, relative to the parent nuclei. This is much greater than the velocity transfer reported by Greiner et al. and may be indicative of new phenomena at this energy.

Description of Experiment

We measured energy and angular distributions of fragments emitted in the collision of 100 MeV/nucleon ^{40}Argon + Uranium. The exposure was made at the Berkeley Bevalac's Irradiation Facility. We used Lexan plastic detectors to measure fragment distributions for $5 \leq Z \leq 10$.

The detector stacks contained between 10 and 400 sheets of 75 micron thick plastic. From previous experience we found that a 10% difference in sheet thickness could cause a 100% change in detection efficiency, especially for particles with low detection efficiency ($\leq$20%). We decided to reduce the seriousness of this problem by pre-selecting our sheets. We measured the thicknesses at four points on each sheet. We rejected sheets if the average thickness or the thickness gradient exceeded a certain limit. Approximately one-third of the sheets were rejected. The stacks were milled to 3" x 3" so that each stack would be of the same area and to facilitate aligning tracks in adjacent sheets.

The stacks were mounted in a frame that fit inside a $8\frac{1}{2}$ foot vacuum chamber. The chamber was two feet in diameter and the stacks were placed at radial distances as far from the beam line as possible to reduce background from beam particles passing through the stacks. The stacks were mounted at angles of 10, 16, 24, 35, 55, 80, 100, 125, 145, 156, 164, and 170 degrees. These angles were chosen so as to optimize the number of stacks that could be fit in the chamber. The angular widths and solid angle for the detectors are listed in Table 1. Two detector stacks were placed at each angle: a thick stack to measure fragments with $5 \leq Z \leq 8$ and a thin stack to measure fragments with $7 \leq Z \leq 10$.

The target was mounted in the middle of the frame at 45° to the beam direction. The frames were segmented into three pieces for ease of transportation and were easily connected at run time. Figure 1 shows the detector configuration. In order to obtain a large dynamic range in cross section we conducted three exposures, each with different beam fluences, target thicknesses, and stack thicknesses. If we were to conduct only a single exposure, then we would not be able to obtain information at high cross section as the track densities in the plastic would be too high to analyze. With a lower beam fluence and a thinner target we can obtain high cross section measurements at low energy with good energy resolution. Table 2A, 2B, and 2C lists the beam fluence, target thickness, and number of sheets per stack for each run. The thick stacks at 10 to 35 degrees could have used about 50 extra sheets as the event rate was still finite at the back of these stacks. We used an excess of sheets at the backward angles. The combination of low cross section and small solid angle in the backward direction led to there only being a few sheets with any events in them.

The beam energy at the entrance to the vacuum chamber was 105 MeV/nucleon. The energy at the center of the thickest target was ~101 MeV/nucleon.

The methods for processing the Lexan have been described elsewhere,[25,26] so only a brief description will be given here. The Lexan was exposed to ultraviolet light and etched in 6.25N NaOH to make tracks visible in a microscope. The tracks were etched long enough so that cylindrical holes would be formed that were detected by passing ammonia gas through the cylinders onto blueprint paper. The

ultraviolet exposure enhanced the sensitivity of the plastic. Two exposures were used. The first was a three day exposure on each side of the sheets which allowed a cylinder to form in the last sheet before the end of the range for charge 5 and above. The second exposure was one day on each side per sheet and was used to detect charge 7 and above. This is useful because at a given range there is usually a much higher density of lighter charges. By going to a shorter UV exposure we can filter them out. The plastic is affected by UV in the 3000 A region. A meter sensitive to UV at 3600 A (mercury has a strong line there) was used to monitor the UV output. The UV bulbs tend to weaken appreciably after 1000 to 2000 hours of use--about the total exposure time needed to process all of the sheets in the experiment. A change in UV output would affect charge assignments and detection efficiencies. We found the bulb output remained constant at the ±10% level. Fluctuations did not seem to affect the results. The etch time for the sheets was 30 hours. In the middle of the experiment it was necessary to change from etching in a small tank to a much larger tank. At this time the etch rate of the plastic changed slightly and the changing of the etch tanks is believed to be the culprit. We accounted for this by making charge assignments and detection efficiency assignments for each bulk etch rate, V_g, separately. The changes were not serious but it took an appreciable amount of time to correct for them.

Etched tracks can be divided into three classes--test tubes, cylinders, and cones--as shown in Fig. 2. When a particle stops in a sheet of plastic, the track can etch to the end of range and then etch at the bulk etch rate of the plastic, leaving a track that looks like

a miniature test tube. Cylinders occur when the track etches through the whole sheet. If the track doesn't etch through the whole sheet a cone pair will appear, one where the particle entered the sheet and another where it exited. A measurement of the length of a cone allows us to compute the etch rate along the track. By measuring the cone length, test tube length, and sheet thicknesses in between the cone sheet and test tube sheet, we can compute the distance from the cone to the end of range of the particle. With a knowledge of the track etch rate, V_T^*, and the average distance to end of range, $\bar{R}$, we can determine the charge of the particle.

It is convenient to redefine the track etch rate as $V_T = V_T^* - V_g$ where V_g, the bulk etch rate of the plastic, is typically about 0.19 microns/hour. Figure 3 shows a plot of V_T^* vs $\bar{R}$ for 400 points. We see that the points lie in distinct bands. From calibrations we know that $V_T \propto \bar{R}^{-1.6}$. We define the range-adjusted track etch rate $V_T(@100\mu) = V_T(\bar{R}) \times (\bar{R}/100)^{1.6}$ to be the measured track etch rate adjusted to 100 microns. We then make histograms (Figs. 4a and 4b) of number of events vs $V_T(@100\mu)$. Distinct charge peaks are seen. The charge assignments are based on ^{12}C, ^{14}N, and ^{20}Ne cyclotron calibrations and on direct observation of ^{8}Li and ^{8}B tracks (via the reactions $^{8}Li \rightarrow {}^{8}Be \rightarrow 2\alpha$ and $^{8}B \rightarrow {}^{8}Be \rightarrow 2\alpha$, which lead to characteristic "hammer tracks").

As a further check on sheet thickness, and as a check on etch conditions, all sheets were weighed before and after etching. Sheet thickness fluctuations were taken into account when computing detection efficiencies. We found that preselecting the sheets greatly reduced the errors due to thickness fluctuations.

We measured approximately 5000 events. Until the measurement process can be fully automated it will be difficult to increase the number of events that can be measured in a single experiment. The total number of data points in the present work is not significantly greater than in refs. 11 and 26 even though our measurements extend over a much wider dynamic range than in our previous experiments. Our data will be more spread out than in previous experiments. This is done so that we may obtain a good overall view of the cross section but at the expense of sacrificing small details in structure. An advantage of our detector is that if we then believe there may be structure somewhere it is usually possible to later process more sheets and investigate the region in more detail.

Experimental Results

We obtained double differential cross sections for the fragments boron, carbon, nitrogen, oxygen, fluorine, and neon. A complete list of results is shown in Table 3. The data are plotted in Figs. 5-10. Some isolated points where there may be only one point at a particular angle or at backward angles where there is a large energy interval are not plotted. The lines drawn through the data are meant only as a guide to the eye.

The data show several interesting characteristics. The boron spectrum at 16 degrees and at energies above 40 MeV/nucleon is nearly flat in contrast to the exponential fall-off seen at larger angles. This may be due to effects of projectile fragmentation. Small energies in the projectile frame are transformed to large values when seen in the lab. The exponential fall-off in the data at large angles is characteristic of fragment distributions seen at higher beam energy. The distributions at 10 degrees clearly show projectile fragmentation peaks at the beam energy/nucleon. Beyond the beam energy/nucleon the cross sections rapidly drop. The distributions for carbon and boron appear to be quite similar in magnitude, but as we go to higher mass the total cross section drops.

Data Analysis

1. Thermal Parametrization of the Data

It is convenient to divide the data into two groups. The first group covers fragments which are presumably emitted in central collisions--low to intermediate energy nuclei emitted at all angles. The second group contains fragments that are apparently from the projectile, which are produced in peripheral collisions and emitted at small laboratory angles with nearly the beam velocity.

Let us assume that fragments are emitted thermally by a moving source. We shall take:

$$\frac{d^2\sigma_i}{dEd\Omega} = \frac{\sigma_i}{2(\pi\tau)^{3/2}} \sqrt{E}\, e^{-E/\tau} \tag{18}$$

to be the non-relativistic Maxwell-Boltzmann distribution in the moving frame for the fragments, where E is the kinetic energy and σ_i is the normalization for the production of the ith fragment. For central collisions, where we expect a large number of nucleons to be found in the source, we may take τ to be the temperature T. For peripheral collisions we take into account two-body kinematics by setting $\tau = \nu T$, with $\nu = A/(A-K)$. This preserves the relation between the Gaussian width, σ, and T (eq. 6), so our discussion of projectile fragmentation will be valid for either the thermal or sudden breakup models. We also expect that the normalization, σ_i, should be "reasonably" related to the partial production cross section for fragment i. As an obvious example, we note the normalization shouldn't exceed the product of the total cross section for the reaction times the number of nucleons in the collision.

A. Fragments Apparently From Central Collisions

Fits using a single source (3 parameters) gave poor results, so two sources (6 parameters) were used. For each source the three parameters were the temperature, $\tau = T$, source velocity, β, and normalization, σ. Since the data cover a large dynamic range, the points that were included in each fit had to be carefully chosen. The procedure was to pick a set of points, determine the best fit using a chi-square minimization routine, and compare the fit to the data. Points that were located far from the fitted curves were rejected and a new fit was made. Usually points would be rejected because they were at small angles and contained contributions from projectile fragmentation. Most of the rejected points were next treated with the projectile fragmentation analysis.

A list of the parameters, χ^2, the number of points fit and the angle and energy constraints were shown in Table 4. The fits for boron, carbon and nitrogen are shown in Figs. 11-13. The slower of the two sources has a velocity $\beta_s \sim 0.07$ and temperature $T_s \sim 27$ MeV. The faster source has a velocity $\beta_f \sim 0.17$ and temperature $T_f \sim 38$ MeV. Note that the values of χ^2, especially for boron, are fairly large. This is mainly due to the large dynamic range being covered. The boron data can be fitted better with the following restrictions: at 16° exclude energies >30 MeV/nucleon; at 24° exclude energies >40 MeV/nucleon; at 35° exclude energies >60 MeV/nucleon. This fit gives a χ^2 of 106 for 33 points. The velocities and temperatures are $\beta_s = 0.0696$, $T_s = 23.2$, $\beta_f = 0.146$, and $T_f = 36.6$. If we exclude all 16° and

24° data from the fit the χ^2 is reduced to 50.9 for 26 points. The fitted velocities and temperatures are $\beta_s = 0.0778$, $T_s = 22.5$, $\beta_f = 0.155$, and $T_f = 35.1$. We see that the value of χ^2 has significantly improved while the source velocities and temperatures have changed only slightly. Similar improvements apply for the carbon and nitrogen data.

We can compare the values of the parameters to those we would expect if either a target explosion or a nuclear fireball is the source of the fragments. For target explosion we assume that the uranium and argon nuclei recoil as a single entity. Energy and momentum conservation give the internal energy, E_{int}, and the recoil velocity, β, of the source. For the nuclear fireball only the participants, that is, the nucleons in the classical overlap region, are involved in the reaction. The participants in the collision at optimal impact parameter, which occurs when the projectile is just totally enclosed by the target ($b = R_{Target} - R_{Projectile}$), give a velocity and temperature that are suitable averages for the fireball model. Target explosion gives β=0.067 and T = 2.8 MeV and the fireball β is approximately 0.15 and T=9.2 MeV for decay to protons. If we assume the recoiling nucleus to be an excited Fermi gas the source temperatures are change to T = 8 MeV for target explosion and T = 17 MeV for the fireball.[27]

We note that the slow source has a velocity corresponding to target explosion while the fast source has a velocity corresponding to the fireball. The source temperatures required to fit the data are much higher than those predicted by either Maxwell-Boltmann or Fermi-Dirac statistics. We see that the problem of

high temperatures seen at projectile energies of 400-500 MeV/nucleon[11] also appears at 100 MeV/nucleon. The anomalously high temperature is also seen at 100 MeV/nucleon for the fireball source. There is no corresponding temperature to compare to for a fireball source of beam energies of 250 and 400 MeV/nucleon for composite fragments as the experimenters either did not report a temperature[14] or did not consider it to be an adjustabie parameter.[11]

There have been several suggestions to explain the discrepancies between the predicted and "measured" source temperatures. We expect that production of composites will decrease the numbers of degrees of freedom of the source, thereby giving a higher temperature. For small increases in temperature this may be a reasonable explanation, but there are many cases where the temperature is a factor of three or more greater than expected. Since most of the emitted fragments are protons and a typical source has more than fifty nucleons, a sufficiently high temperature system to fit the data cannot be built by the creation of a few composite particles.

Pre-equilibrium and nonthermal emission are also possible explanations of the high apparent temperatures. J. Stevenson has examined several mechanisms of nonthermal emission, including rotating and expanding sources.[26] He has found that these mechanisms do not give a satisfactory fit to the data for 500 MeV Ar + Au interactions.

Since the excitation energies are small we should check to see how well the data are fitted by a Fermi-Dirac distribution as

opposed to a Maxwell-Boltzmann distribution. Most of the fragments we see have kinetic energies exceeding the nuclear Fermi energy, so we would not expect much difference between a Maxwell-Boltzmann fit and a Fermi-Dirac fit. For carbon the Maxwellian fit gives a χ^2 of 30 for 25 points, with $\beta_s = 0.075$, $T_s = 28.1$, $\beta_f = 0.17$, and $T_f = 39.2$. The Fermi-Dirac fit is made using:

$$\frac{d^2\sigma}{dEd\Omega} = \frac{\sigma_i}{2(\pi\tau)^{3/2}} \frac{1}{1+e^{(E-\mu)/\tau}} \tag{19}$$

where μ is the chemical potential at temperature $\tau = T$. The fit gives $\chi^2 = 26$, $\beta_s = 0.079$, $T_s = 28.2$, $\beta_f = 0.17$, and $T_f = 39.2$. The χ^2 drops slightly and there is negligible change in the fitted parameters.

B. Projectile Fragmentation

The projectile fragmentation peaks are broad and asymmetric. Since definite peaks are seen only at 10°, several different sets of parameters give fits of comparable quality. The data are insufficient to allow firm conclusions to be drawn.

Let us consider the oxygen data for energies greater than 40 MeV/nucleon. Viyogi et al.[28] measured a projectile fragmentation temperature of ≈8 MeV for 213 MeV/nucleon Ar + U, for fragments emitted from zero to four degrees. They measured a partial cross section of ~81 mb for oxygen production. We can check to see if the results of Viyogi et al. apply to our data. Figure 14a shows how a source with T = 8 MeV, $\beta = 0.43$ (corresponding to a beam energy of 100 MeV/nucleon) would appear using the values of the partial cross sections for oxygen isotopes reported by Viyogi et al. We see that the fit is very poor. Different

parameters will be required to fit the data. If the partial cross sections are kept the same, but the temperature T is raised to 15 MeV (Fig. 14b), the peak is picked up fairly well. Similar results apply when examining the fluorine and neon distributions. The data at 16° are obviously not fitted at all; they will require a two-source model for a fit. The difference between our results and those of Viyogi et al. may be explained either by supposing that because we cannot observe angles less than 10° we are measuring the wings of some distributions, or that the temperature (or equivalently the momentum width) may rise in the vicinity of 100 MeV/nucleon.

Before considering multi-parameter fits we must check to see how sensitive the fits are to the effects of isotope distribution and target thickness. If the assumed isotope distribution varies from the true one, there will be a misassignment of fragment energy. The beam loses ~10 MeV/nucleon traveling through the thickest target and this will have an effect on the measured cross sections. Figure 15 shows the results of these effects. In Fig. 15a, an ^{16}O distribution with a correction for finite target thickness is compared to an ^{16}O distribution with no target thickness correction. In Fig. 15b, an oxygen distribution with T = 15 MeV using the isotope distribution of Viyogi et al. is compared with a pure ^{16}O distribution. We see in both cases that the discrepancies are within the error bars of the data (Fig. 8). Using ^{16}O as the only oxygen present with no target thickness correction will not significantly alter the results. (Effects of isotopes and target thickness have also been checked for the

"central collision" data and have also been found to be small.)

To fit the oxygen data well with thermal models at energies greater than 40 MeV/nucleon it is necessary to increase the number of parameters. One way to do this is to assume that there are two fast sources (Fig. 16a). The fit gives $\chi^2 = 13$ for 20 points. The values of the fitted parameters are $\sigma_1 = 12500$ μb, $\beta_1 = 0.424$, $\tau_1 = 15$ MeV (corresponding to T = 24 MeV or a momentum width of 151 MeV/c), $\sigma_2 = 1200$ μb, $\beta_2 = 0.338$ and $\tau_2 = 34.8$ MeV. The first source has nearly the beam velocity and a temperature much higher than that expected for conventional projectile fragmentation. The second source has a very high τ_2, but we are unsure of its nature, so it would be incorrect to assign it a temperature. The second source appears as if some piece of the projectile underwent a collision with the target nucleus with a resulting large transfer of momentum. This may not be the correct interpretation because the fact that the intermediate rapidity points can be fitted by a thermal source may be an accident.

The nitrogen data have also been fitted at 10° and 16° (Fig. 16b). The results are $\chi^2 = 19.8$ μb for 17 points, $\sigma_1 = 4110$ μb, $\beta_1 = 0.416$, $\tau_1 = 20.6$, $\sigma_2 = 2760$ μb, $\beta_2 = 0.328$, $\tau_2 = 20.6$ μb. Points with energies greater than 45 MeV/nucleon were included in the fit. The fit does not reproduce the peak at 10°, but the error bars in the data are fairly large. Note that at 24° the fit exceeds the data. This increases our suspicion that the large momentum transfer source may be fictitious.

The boron and carbon data that appeared to be due to projectile fragmentation were fitted at 16° and 24°. Two fast sources were necessary to obtain reasonable fits. For boron the best fit gives $\chi^2 = 10.8$ for 16 points, $\sigma_1 = 6.84 \times 10^8$, $\beta_1 = 0.424$, $\tau_1 = 5.4$ ($T = 7.4$), $\sigma_2 = 13600$, $\beta_2 = 0.288$, $\tau_2 = 41.6$ (Fig. 17a). The fit overshoots the data at 35°. The normalization cross section σ_1 for the beam velocity source is far too high. By raising the temperature we can lower the normalization. A fit with the parameters $\sigma_1 = 543$, $\beta_1 = 0.424$, $\tau_1 = 11$ ($T = 15.2$), $\sigma_2 = 133300$, $\beta_2 = 0.284$, and $\tau_2 = 43.2$ gives a χ^2 of 15.2 (Fig. 17b). The figure shows that the fit is still reasonably good although the problems at 35° have not been settled. The carbon is fit at 16° and 24° for energies above 50 MeV/nucleon. We obtain $\chi^2 = 11.3$ for 16 points, $\sigma_1 = 44300$ μb, $\beta_1 = 0.402$, $\tau_1 = 16.4$ ($T = 23.4$), $\sigma_2 = 7060$ μb, $\beta_2 = 0.276$, and $\tau_2 = 45$ (Fig. 18). Note that the fit is close to the 10° points and is roughly equal to the data at 35°, which was fitted with the fireball source. A summary of the projectile fragmentation fits is given in Table 5.

i) Coulomb Scattering

We should check to see what effect Coulomb scattering has on the transverse momentum transfer. Suppose two nuclei collide with charge and mass Z_1, A_1 and Z_2, A_2. The half distance of closest approach in a head-on collision is given by:

$$a = \frac{Z_1 Z_2}{2E_{cm}} \qquad (20)$$

We take the radius:

$$R = r_o(A_1^{1/3} + A_2^{1/3}) \tag{21}$$

where $r_o = 1.2 \times 10^{-13}$ cm. The critical scattering angle in the center of mass, which occurs when the nuclei just touch, is given by:

$$\sin \frac{\theta_c}{2} = \frac{a}{R-a} \tag{22}$$

For ^{40}Ar on ^{238}U at 100 MeV/nucleon $\theta_c \sim 3.5$ degrees. From $\sin\theta_c \sim 0.06$ and the beam momentum of 443 MeV/c/nucleon we have a transverse momentum transfer of approximately 27 MeV/c/nucleon. For an ^{16}O fragment this gives a momentum transfer of 432 MeV/c. The measured σ is 475 MeV/c, so the widths have a sizable Coulomb scattering component.

ii) Summary of Intermediate and Projectile Velocity Data

The data show that some fragments are seen that are emitted by a source moving at the projectile velocity but the data really are not detailed enough to draw additional conclusions. The source moving at the projectile velocity may have a temperature in excess of the 8 MeV temperature seen in conventional projectile fragmentation, but this may be due to the Coulomb scattering. Data at several angles are needed to resolve the issue. The data at intermediate energy are consistent with emission from a source moving at $\beta \approx 0.1$ in the projectile frame with a high τ, but this may only be an exercise in curve fitting, as the fits often overshoot data at larger angles.

2. Fireball Model

Although the data are not fitted by a source with a

temperature and velocity both corresponding to what would be expected from the nuclear fireball model, it is still a good idea to see how the model compares with the data. There are several levels of complexity one can have in developing a model to describe emission of the fragments we see. I have developed a fairly simple model which can be compared with the data.

The model follows the general procedure of the ordinary fireball model. Ten equally spaced values of impact parameter are chosen. The integrals that give the number of projectile and target participants are easily evaluated by a Monte Carlo calculation.[18] Energy and momentum conservation give the momentum and excitation energy, E^*, of the recoiling fireball. We assume that the fireball of mass A breaks into two fragments of mass K and A-K, and the fragment of mass A-K decays to nucleons. A nuclear binding energy correction is made by subtracting 8x(A-K) from the excitation energy. For a Maxwell-Boltzmann gas the temperature of the fireball is given by:

$$T = \frac{2}{3}\frac{(E^*-8(A-K))}{(A-K+1)} \qquad (23)$$

as there are (A-K+1) particles in the system. If the fragment mass is greater than the number of nucleons in the fireball, the contribution at that impact parameter is neglected. The number of participants and the fireball velocities and temperatures for each impact parameter are shown in Table 6. We see that at the largest impact parameter the temperature shows a dramatic increase due to the small number of nucleons in the fireball. Recoil corrections (such as from two-body kinematics) will lessen this effect. We might suspect that this may be the source of the high temperatures seen in the data, but we must not

forget that fragments emitted from sources moving at the target explosion velocity are formed in systems made of large numbers of nucleons. In this model the fireball decays according to a Maxwell-Boltzmann distribution, and the results are integrated over impact parameter and transformed to the laboratory frame. Recoil corrections to the fireball are not taken into account. There is no special weighting (other than geometric) of impact parameter, although the data suggest that impact parameters near zero should be neglected. The results for production of carbon fragments are shown in Fig. 19. The fit is normalized to fit the data at 24° at 51 MeV/nucleon. The fit is unacceptably poor. This shows either that models of the fireball type are not useful or that more sophisticated models need to be used.

3. Invariant Cross Section and Exponential in Momentum

Contours of invariant cross section ($f = \frac{1}{p}\frac{d^2\sigma}{dEd\Omega}$) for boron are shown in Fig. 20. The coordinate axes are parallel and transverse momentum. The curves are obtained by drawing smooth curves through the data, rather than corresponding to specific data points. The contours are roughly circular with centers around a parallel momentum, $p_{\parallel}$, of about 1000 MeV/c. For large $p_{\parallel}$ the contours deviate from being circles due to effects of projectile fragmentation.

In the case of isotropic emission from a moving frame the contours form ellipses with $p_{\parallel}$ being one of the axes. For low source velocities $\beta_o << 1$ these ellipses should be nearly circles. From locations of the centers of the circles we obtain the velocity of the source:

$$\beta_o = \frac{p_{\parallel}}{M\gamma_o} \approx \frac{p_{\parallel}'}{M} \qquad (24)$$

and from the radii of the circles we obtain the velocities β' of the fragments in the moving frame:

$$\beta' = \frac{p'}{M\gamma'} \approx \frac{p'}{M} \tag{25}$$

We should note that these velocities refer to averages and are not representative of discrete sources.

Best fit circles were constructed for the invariant cross section contours using a χ^2 minimization routine. Both β_o and β' were varied until the minimum χ^2 was found. Selected points, usually those at small angle and large $p_{||}$, were excluded from the fits if they caused the contours to deviate seriously from being circular. A scatter plot of β_o vs β' for the fragments boron through nitrogen is shown in Fig. 21. We note there is some correlation between β_o and β'. The correlation appears poor here because there is still some contamination from projectile fragments at small angles. The graph looks much better if these contaminants are removed. The dependence of β' and β_o has been studied for a number of experiments by Price and Stevenson.[29] They claim that the correlation of fragment velocity with source velocity independent of fragment mass shows that the source cannot be thermal in nature.

From the constructed circles we can determine the momentum, p', of the fragments in the moving frame, and plot the values of p' as a function of invariant cross section (Fig. 22). The points shown in the figure are obtained from the boron, carbon, and nitrogen data. Contributions from projectile fragmentation are not included. Recall that the points are not data points but are obtained by drawing smooth curves through the data. Overlaid on the plot are curves for the

reactions 400 MeV/nucleon Ne + U → ^{8}Li and boron.[12] The curve for ^{8}Li is shown multiplied by three as an approximate correction for the other lithium isotopes. The plotted points surprisingly follow the pattern of the universal curve of Price et al.[12] The characteristic momentum of the plotted points is approximately P_c = 190 MeV/c. This compares to P_c = 236 MeV/ for 400 MeV/nucleon Ne + U and P_c = 340 MeV/c for 500 MeV/nucleon Ar + Au. Since all curves lie relatively "close" to one another this suggests that when comparing several curves, a change in slope (P_c) is compensated by a change in normalization (K) for some distribution $f = Ke^{-P/P_c}$. Alternatively, we might say that at some value of momentum in the moving frame, all invariant cross sections are basically identical, with the first order corrections being determined by P_c.

The origins of the universal curve still remain unknown. It is surprising that fragment data from reactions for projectile energies of 100 to 2100 MeV/nucleon all lie close to the same curve.

4. Friction Model

Let us consider what the friction model of Abul-Magd et al.[20] predicts at 100 MeV/nucleon. In my experiment the ^{40}Ar is fragmented to less than one-half its original size and the projectile fragmentation peaks are poorly resolved, so the best we should hope for are order of magnitude agreements of the theory with the data.

At an incident energy of 100 MeV/nucleon, π_o is 443 MeV/c. Rather than using an expansion to solve for $q_{\parallel}$ and η (eq. 15) we solve for $q_{\parallel}$ and then identify:

$$\eta = \frac{-\langle q_{\parallel} \rangle}{\langle \vec{q}^2/2m \rangle} - 1 \qquad (26)$$

From eq. 14 we obtain:

$$q_{\parallel} = \frac{1}{2\pi_o} \{(\frac{\vec{q}^2}{2m})^2 - \vec{q}^2 - 2(\frac{\vec{q}^2}{2m})(m^2+\pi_o^2)^{\frac{1}{2}}\} \qquad (27)$$

Using $\frac{\vec{q}^2}{2m}$ = 80 MeV (which properly should be used only above 500 MeV/nucleon)[30] gives $q_{\parallel}$ = -347 MeV/c and η = 3.3. Note that η is approximately eight times larger than at 2 GeV/nucleon. Because of the large value of η at 100 MeV/nucleon we may have a sensitive test of the friction model. With η = 3.3 and $\langle U \rangle \leq$ 50 MeV we have $|\langle P_{\parallel} \rangle| \leq$ 108 MeV/c. For fragmentation to ^{16}O, the moving source velocity is 0.424 which gives a momentum transfer of 90 MeV/c. This is reasonably close to the predicted value although it only applies to single nucleon removal.

Let us next consider the prediction of eq. 16. Using σ_o = 150 MeV/c for fragmentation to ^{16}O we get $\langle P_{\parallel} \rangle \approx$ 520 MeV/c in the pure abrasion approximation. This is somewhat larger than expected. A full abrasion-ablation calculation will reduce this value.

5. Asymmetry of the Projectile Fragmentation Curves

The projectile fragmentation data at 10° show a marked asymmetry. The high energy side is much steeper than the low energy side of the projectile fragmentation peak. Such asymmetric peaks have previously been observed at lower beam energies.[31] The asymmetry is obviously due to projectile interaction with the target.

Predicting the shape of the peak is obviously a difficult problem. Rather than attempting to obtain the shapes of the peaks, I have developed a simple model that suggests how the peaks may be explained. If the model proves to be useful it can be further developed to try to understand the data. The model assumes that some fraction of the

target nucleons, which are physically near the projectile, will have N nucleons within the Fermi sphere in momentum space of the projectile nucleus, which contains A nucleons. We note that this model will obviously not work at higher projectile energies. The resulting configuration of A + N nucleons can then fragment to a fragment of mass K.

The calculation proceeds as follows. For a ^{238}U target we arbitrarily assume that 10% (i.e. 24) of them can interact with the projectile. These 24 nucleons are given momenta randomly drawn from a Fermi distribution. The A nucleons of the projectile are also given momenta drawn from a Fermi distribution. The momenta of the target nucleons are transformed to the projectile frame. If the resulting momentum of a nucleon is less than the Fermi momentum (taken to be 250 MeV/c) then it is allowed to join with the projectile nucleus. Usually N = 0 or 1 for the system described. We then randomly pick out K nucleons from the resulting system of A + N nucleons. The parallel and transverse momenta of the fragment are computed. For the present we do not constrain the projectile to have zero momentum in its rest frame. The effect will be that of emission from an infinitely heavy nucleus. The calculation is repeated many times until sufficient statistics are obtained. We take the beam momentum to be in the z-direction. The x and y distributions are then expected to be Gaussian distributed about zero momentum. The expected asymmetry will then show up in the negative z direction.

We first do the calculation for two cases, where a 100 MeV/nucleon projectile of mass 40 fragments with emission of (a) a mass 3 fragment and (b) a mass 16 fragment, with 24 nucleons contributing from the target (Fig. 23). The distributions of parallel (z-direction)

momentum and of transverse momentum in the x or y direction are shown in the projectile frame. We see in both cases that sufficiently far on the tails of the distributions the longitudinal distribution exceeds the transverse by a factor of 2 or more. Nearer to zero momentum there is not a great difference between the parallel and transverse distributions, and further refinements or a different model will be necessary to explain the shapes of the experimental distributions. In Fig. 24 is shown the calculation for a 20 MeV/nucleon projectile fragmenting to a mass 3 nucleus. There is a pronounced effect for all momenta less than zero as the target and projectile Fermi spheres are much closer than at 100 MeV/nucleon.

The model can be improved by placing constraints on the momentum of the projectile nucleus. We form the total momentum from the vector sum of the assigned momenta of the individual nuclei. If the components of total momentum and the magnitude exceed a certain value, then that combination is rejected and a different set is selected. Figure 25 shows the momentum distribution for a mass-16 nucleus with no momentum constraint and with the constraint that each momentum component be less than 30 MeV/c and total momentum less than 40 MeV/c. In this calculation there is no contribution from the target. The histograms have the same areas. We see that the momentum-constrained distribution is narrower than the unconstrained distribution. The unconstrained distribution has a σ of 470 MeV/c which is what we expect for emission from ar infinite nucleus. The constrained distribution should have a width of 290 MeV/c. The calculation gives a width of 360 MeV/c. The width could be made smaller by using tighter constraints, but this would take an excessive amount of computer time.

We would have to find a different algorithm for selecting the momentum to obtain a significant improvement in the width. Using the above momentum constraints, we obtain the distributions for fragmentation to ^{16}O from 100 MeV/nucleon ^{40}Ar with the interaction of 24 target nucleons (Fig. 26). Comparing this caluclation to the one with no momentum constraints, we see there is a slight improvement in longitudinal vs transverse counts. At a momentum of -1200 MeV/c the longitudinal to transverse ratio is 2.6:1 for the momentum-constrained distribution while it is 1.6:1 for the unconstrained distribution. As we go further out in negative momentum the difference in the ratios of the two distributions becomes more significant.

These calculations show we may have a process that generates asymmetric tails. One way to check the calculation with experiment would be to compare with projectile fragmentation data for only the removal of a few nucleons from a large projectile. In this case we would not have to use the constraints of momentum conservation and the calculation could be done rapidly.

It is important to note that we have analyzed a situation where a rare process (projectile pickup of one or two nucleons) can have a major effect on the tail of a distribution, while the rest of the distribution is essentially unchanged. This should serve notice that we should be wary in applying interpretations based on a distribution's tail to the distribution as a whole.

Summary and Conclusions

Data from the reaction 100 MeV/nucleon Ar + U → fragments have been presented. By conducting three exposures using different combinations of target thickness and beam fluence, we have been able to measure cross sections over a wide dynamic range. Fragments emitted from both central and peripheral collisions are observed.

The data have been fit with thermal sources, each moving with a characteristic velocity and temperature. These sources are not discrete, but are believed to be in some sense an average over a continuum of sources. The data which are apparently due to central collisions can be interpreted in terms of emission of fragments from two sources, one corresponding to a system undergoing "target explosion" and the second from a nuclear fireball. The observed temperatures are higher than one would calculate using energy and momentum conservation and either Fermi-Dirac or Maxwell-Boltzmann statistics. The process that produces these fragments appears to be of the same type that produces "slowly moving, highly excited nuclear matter" which is observed at beam energies of 400 and 500 MeV/nucleon, although its origin remains a mystery. A crude fireball model is developed but it agrees poorly with the data. An improved fireball or firestreak calculation could provide a better fit, but it is likely that it would still be a poor fit. The data lie on a previously discovered universal curve (or better termed "localized region") of invariant cross section vs momentum. The universal curve now encompasses fragments emitted in high energy heavy ion collisions for beam energies from 100 to 2100 MeV/nucleon.

The data which are apparently due to peripheral collisions have

temperatures (or equivalently, widths) exceeding those seen in other projectile fragmentation studies. This may be due either to phenomena peculiar to 100 MeV/nucleon, to Coulomb scattering or to a peculiarity of looking at the tail of the projectile fragmentation distribution. We showed that 100 MeV/nucleon is a good energy to test the predictions of the friction model of projectile fragmentation, although the results of this experiment are not well suited at present as a test of the model. We suggested a model that allows part of the target nucleus to participate in projectile fragmentation. Further developments are needed before it can be compared with data. Preliminary results show that the longitudinal distribution of projectile fragments (when viewed in the laboratory frame) can have an enhanced low energy tail. The calculation is illustrative of a situation where an apparently small effect can have a dramatic influence on the tail of a distribution while having a negligible effect on the bulk of it.

We see that the problems encountered in analyzing the data for experiments at 400 and 500 MeV/nucleon are apparent at 100 MeV/nucleon. Correlation experiments could help determine if thermal equilibrium is reached before fragments are emitted from central collisions. Further theoretical developments are necessary before the interactions of relativistic heavy ions can be fully understood.

References

1. For a recent review, see A.S. Goldhaber and H.H. Heckman, Ann. Rev. Nuc. Sci. 28, 161 (1978).
2. A. Poskanzer, Nature 278, 17 (1979).
3. J. Stevenson, Phys. Rev. Lett. 41, 1702 (1978).
4. Z. Fraenkel and Y. Yariv, unpublished.
5. R.K. Smith and M. Danos, in Proceedings of the Topical Conference on Heavy-Ion Collisions, Fall Creek Falls State Park, Pikeville, Tennessee, 1977, CONF 77-602, p. 363.
6. J. Gosset, J.I. Kapusta, and G.D. Westfall, Phys. Rev. C18, 844 (1978).
7. A.A. Amsden, A.S. Goldhaber, F.H. Harlow, and J.R. Nix, Phys. Rev. C17, 2080 (1978).
8. A.S. Goldhaber, Phys. Lett. 53B, 306 (1974).
9. A. Mekjian, Phys. Rev. Lett. 38, 640 (1977).
10. H.H. Gutbrod, A. Sandoval, P.J. Johansen, A.M. Poskanzer, J. Gosset, W.G. Meyer, G.D. Westfall, and R. Stock, Phys. Rev. Lett. 37, 667 (1976).
11. J. Stevenson, P.B. Price, and K. Frankel, Phys. Rev. Lett. 38, 1125 (1977).
12. P.B. Price, J. Stevenson, and K. Frankel, Phys. Rev. Lett. 39, 177 (1977).
13. G.D. Westfall, J. Gosset, P.J. Johansen, A.M. Poskanzer, W.G. Meyer, H.H. Gutbrod, A. Sandoval, and R. Stock, Phys. Rev. Lett. 37, 1202 (1976).
14. J. Gosset, H.H. Gutbrod, W.G. Meyer, A.M. Poskanzer, A. Sandoval,

R. Stock, and G.D. Westfall, Phys. Rev. C16, 629 (1977).

15. M. Ta Cheung and E. Moeller, Phys. Rev. Lett. 41, 1352 (1978).

16. D.E. Greiner, P.J. Lindstrom, H.H. Heckman, B. Cork, and F.S. Bieser, Phys. Rev. Lett. 35, 152 (1975).

17. H. Feshbach and K. Huang, Phys. Lett. 47B, 300 (1973).

18. J. Stevenson, unpublished.

19. G.D. Westfall, R.G. Sextro, A.M. Poskanzer, A.M. Zebelman, G.W. Butler, and E.K. Hyde, Phys. Rev. C17, 1368 (1978).

20. A. Abul-Magd, J. Hüfner, and B. Schurman, Phys. Lett. 60B, 327 (1976).

21. P.J. Siemens and J.O. Rasmussen, Phys. Rev. Lett. 42, 880 (1979).

22. K.L. Wolf, H.H. Gutbrod, W.G. Meyer, A.M. Poskanzer, A. Sandoval, R. Stock, J. Gosset, C.H. King, G. King, Nguyen Van Sen, and G.D. Westfall, Phys. Rev. Lett. 42, 1448 (1979).

23. S. Nagamiya, L. Anderson, W. Brückner, O. Chamberlain, M-C. Lemaire, S. Schnetzer, G. Shapiro, H. Steiner, and I. Tanihata, Phys. Lett. 81B, 147 (1979).

24. R. Kullberg and A. Oskarsson, Cosmic and Subatomic Physics Report LUIP 7803 (1978).

25. R.L. Fleischer, P.B. Price, and R.M. Walker, Nuclear Tracks in Solids: Principles and Applications, University of California Press (1975).

26. J. Stevenson, LBL-7192 (Ph.D. thesis) (1977).

27. E.C. Stoner, Philosophical Magazine 28, 257 (1939).

28. Y.P. Viyogi, T.J.M. Symons, P. Doll, D.E. Greiner, H.H. Heckman, D.L. Hendrie, P.J. Lindstrom. J. Mahoney, D.K. Scott, K Van Bibber, G.D. Westfall, H. Wieman, H.J. Crawford, C. MacParland,

and C.K. Gelbke, Phys. Rev. Lett. 42, 33 (1979).

29. P.B. Price and J. Stevenson, Phys. Lett. 78B, 197 (1978).

30. O. Benary, L.R. Price, and G. Alexander, UCRL-20000 NN.

31. C.K. Gelbke, in 4th High Energy Heavy Ion Summer Study, Lawrence Bekeley Laboratory, Berkeley, California, 1978, LBL-7766.

Table 1

Angular Width and Solid Angle of the Detector Stacks

Angle θ, Degrees	Angular Width, Degrees	Solid Angles, Msr
10	±1.8	4.0
16	±2.6	8.5
24	±3.9	18.
35	±5.4	35.
55	±7.6	72.
80	±9.9	120.
100	±9.9	120.
125	±7.6	72.
145	±5.4	35.
156	±3.9	18.
164	±2.6	8.5
170	±1.8	4.0

Table 2

Beam Fluence, Target Thickness and Number of Lexan Sheets Per Stack for Each Run

Run A

Beam Fluence = 1.1×10^{12} ions

Uranium Target Thickness = 0.239 gm/cm^2

Polar Angle θ	Azimuthal Angle $\phi = 0$ No. of sheets	Angle $\phi = 30$ No. of sheets
10	50	400
16	50	400
24	50	250
35	40	200
55	40	200
80	40	200
100	40	200
125	40	200
145	30	100
156	30	50
164	30	50
170	30	50

Run B

Beam Fluence = 1.1×10^{11} ions

Uranium Target Thickness = 0.0989 gm/cm^2

Polar Angle θ	Azimuthal Angle $\phi = 0$ No. of sheets	Angle $\phi = 30$ No. of sheets
10	20	50
16	20	50
24	20	50
35	20	40
55	20	40
80	20	40
100	20	40
125	20	40
145	20	20
156	20	20
164	20	20
170	20	20

Run C

Beam Fluence = 1.1×10^{10} ions

Uranium Target Thickness = 0.0491 gm/cm^2

Polar Angle θ	Azimuthal Angle $\phi = 0$ No. of sheets	Angle $\phi = 30$ No. of sheets
10	10	20
16	10	20
24	10	20
35	10	20
55	10	20
80	10	20
100	10	20
125	10	10
145	10	10
156	10	10
164	10	10

Table 3

Data

E+ and E- define the upper and lower limits of the energy interval over which the cross section was averaged. σ+ and σ- are 68% confidence limits on the cross section.

BORON

Angle (deg)	Energy E (MeV/ nuc)	E+ (MeV/ nuc)	E- (MeV/ nuc)	Cross Section σ (μb/MeV-sr)	σ+ (μb/MeV-sr)	σ- (μb/MeV-sr)
16.	10.5	12.1	8.8	4.88E+02	7.29E+02	3.19E+02
16.	19.6	21.1	18.2	3.98E+02	5.80E+02	2.68E+02
16.	23.5	25.3	21.8	1.42E+02	1.81E+02	1.12E+02
16.	31.7	33.2	30.2	1.27E+02	1.65E+02	9.74E+01
16.	49.3	51.7	46.9	3.40E+01	4.24E+01	2.71E+01
16.	60.9	63.2	58.7	3.23E+01	4.18E+01	2.47E+01
16.	71.0	73.2	68.8	1.44E+01	1.89E+01	1.08E+01
16.	76.6	78.7	74.4	1.58E+01	2.02E+01	1.23E+01
16.	81.8	84.0	79.7	2.89E+01	3.32E+01	2.45E+01
16.	88.5	90.6	86.3	2.73E+01	3.13E+01	2.32E+01
16.	93.2	95.4	91.1	2.29E+01	2.67E+01	1.91E+01
16.	97.7	100.0	95.5	1.55E+01	1.82E+01	1.28E+01
16.	102.0	104.0	99.9	1.30E+01	1.53E+01	1.07E+01
24.	10.4	11.9	8.8	5.36E+02	6.23E+02	4.49E+02
24.	19.3	20.4	18.2	2.78E+02	3.78E+02	2.02E+02
24.	23.4	25.0	21.8	7.83E+01	1.06E+02	5.68E+01
24.	29.7	31.2	28.3	2.97E+01	4.32E+01	2.00E+01

Angle (deg)	Energy E (MeV/ nuc)	E+ (MeV/ nuc)	E- (MeV/ nuc)	Cross Section σ (μb/MeV-sr)	σ+ (μb/MeV-sr)	σ- (μb/MeV-sr)
24.	43.8	46.1	41.4	1.25E+01	1.39E+01	1.11E+01
24.	49.1	51.4	46.9	1.46E+01	1.69E+01	1.23E+01
24.	54.0	56.2	51.9	9.65E+00	1.10E+01	8.27E+00
24.	60.6	62.9	58.7	7.63E+00	8.89E+00	6.38E+00
24.	65.0	67.1	62.9	6.79E+00	7.67E+00	5.90E+00
24.	71.1	73.1	69.0	3.26E+00	4.39E+00	2.40E+00
24.	77.0	81.3	72.6	1.78E+00	2.22E+00	1.42E+00
35.	23.3	24.8	21.8	6.41E+01	7.28E+01	5.55E+01
35.	28.5	29.9	27.1	2.56E+01	3.35E+01	1.94E+01
35.	42.2	45.8	38.5	2.94E+00	3.30E+00	2.59E+00
35.	49.0	51.1	46.9	1.11E+00	1.55E+00	7.77E-01
35.	60.4	62.6	58.2	1.65E-01	2.95E-01	8.60E-02
35.	68.6	71.0	66.1	5.76E-02	1.03E-01	3.01E-02
55.	10.4	11.9	8.8	2.26E+02	2.60E+02	1.92E+02
55.	17.3	18.7	15.8	4.93E+01	6.56E+01	3.67E+01
55.	18.2	20.0	16.4	3.13E+01	3.92E+01	2.48E+01
55.	23.4	25.0	21.8	7.34E+00	9.43E+00	5.67E+00
55.	31.4	34.0	28.7	1.02E+00	1.17E+00	8.78E-01
55.	37.6	40.2	35.0	2.13E-01	3.81E-01	1.11E-01
55.	42.3	46.3	38.2	8.04E-02	1.13E-01	5.65E-02
55.	46.1	49.0	43.1	2.88E-02	4.83E-02	1.64E-02
80.	10.8	12.8	8.8	5.25E+01	6.26E+01	4.24E+01
80.	13.6	15.7	11.5	9.77E+00	1.31E+01	7.19E+00
80.	18.8	21.2	16.4	1.51E+00	2.20E+00	1.02E+00

Angle (deg)	Energy E (MeV/ nuc)	E+ (MeV/ nuc)	E- (MeV/ nuc)	Cross Section σ (μb/MeV-sr)	σ+ (μb/MeV-sr)	σ- (μb/MeV-sr)
100.	8.8	11.0	6.6	1.60E+01	2.05E+01	1.25E+01
100.	10.8	12.7	8.8	9.67E+00	1.62E+01	5.50E+00
100.	12.0	15.2	8.8	6.14E+00	6.93E+00	5.34E+00
100.	14.8	17.2	12.3	3.57E-01	5.09E-01	2.46E-01
100.	19.5	24.6	14.5	8.77E-02	1.14E-01	6.73E-02
100.	21.4	26.4	16.4	1.73E-02	3.10E-02	9.03E-03
100.	22.7	27.8	17.6	1.03E-02	1.64E-02	6.22E-03
125.	10.3	12.8	7.8	3.01E-01	5.93E-01	1.37E-01
125.	13.3	17.9	8.8	1.46E-01	2.05E-01	1.03E-01
125.	14.1	18.5	9.8	8.65E-02	1.55E-01	5.49E-02
125.	15.5	20.3	11.5	1.08E-02	2.13E-02	5.88E-03
145.	11.3	16.1	6.6	2.62E-01	3.29E-01	2.08E-01
145.	12.6	17.4	7.8	3.62E-02	6.48E-02	1.89E-02
156.	10.6	16.0	5.2	5.94E-01	7.03E-01	4.86E-01
164.	11.0	16.8	5.2	3.87E-01	5.63E-01	2.60E-01
170.	10.1	16.9	3.3	4.60E+00	5.75E+00	3.45E+00

CARBON

Angle (deg)	Energy E (MeV/ nuc)	E+ (MeV/ nuc)	E- (MeV/ nuc)	Cross Section σ (μb/MeV-sr)	σ+ (μb/MeV-sr)	σ- (μb/MeV-sr)
10.	112.8	115.5	110.1	3.71E+01	4.34E+01	3.07E+01
10.	119.8	122.5	117.1	4.24E+01	4.98E+01	3.50E+01
16.	12 2	14.2	10.3	6.01E+02	7.03E+02	5.00E+02
16.	22.9	24.6	21.2	1.33E+02	1.86E+02	9.35E+01
16.	27.4	29.5	25.4	1.14E+02	1.30E+02	9.88E+01
16.	36.9	38.7	35.2	7.16E+01	8.37E+01	5.95E+01
16.	57.5	60.3	54.6	1.71E+01	1.98E+01	1.44E+01
16.	71.1	73.8	68.4	1.76E+01	2.11E+01	1.41E+01
16.	82.9	85.5	80.3	1.25E+01	1.43E+01	1.08E+01
16.	89.5	92.0	86.9	1.36E+01	1.53E+01	1.18E+01
16.	95.6	98.2	93.1	9.14E+00	1.05E+01	7.79E+00
16.	103.5	106.0	100.9	5.62E+00	6.61E+00	4.62E+00
16.	109.0	111.6	106.5	2.38E+00	3.24E+00	1.73E+00
16.	114.3	117.0	111.7	1.26E+00	1.69E+00	9.27E-01
24.	12.1	14.0	10.3	4.34E+02	4.75E+02	3.92E+02
24.	22.5	23.8	21.2	8.13E+01	1.16E+02	5.61E+01
24.	27.3	29.2	25.4	3.80E+01	4.86E+01	3.07E+01
24.	34.6	36.3	32.9	1.22E+01	1.66E+01	8.85E+00
24.	51.1	53.8	48.3	5.45E+00	5.95E+00	4.95E+00
24.	57.3	59.9	54.6	2.46E+00	3.08E+00	1.95E+00
24.	63.0	65.6	60.4	2.76E+00	3.16E+00	2.36E+00

Angle (deg)	Energy E (MeV/ nuc)	E+ (MeV/ nuc)	E- (MeV/ nuc)	Cross Section σ (μb/MeV-sr)	σ+ (μb/MeV-sr)	σ- (μb/MeV-sr)
24.	70.9	73.4	68.4	1.17E+00	1.50E+00	9.01E-01
24.	75.8	78.3	73.4	9.53E-01	1.21E+00	7.53E-01
24.	83.0	85.4	80.6	6.26E-01	9.11E-01	4.21E-01
24.	87.1	89.6	84.5	3.14E-01	4.33E-01	2.28E-01
24.	92.5	95.3	89.8	2.52E-01	3.53E-01	1.77E-01
35.	12.0	13.8	10.3	3.24E+02	4.41E+02	2.35E+02
35.	20.4	21.7	19.1	4.50E+01	6.92E+01	2.84E+01
35.	27.2	29.0	25.4	1.90E+01	2.16E+01	1.65E+01
35.	33.2	34.8	31.6	7.07E+00	9.31E+00	5.32E+00
35.	49.2	53.4	44.9	6.16E-01	7.03E-01	5.29E-01
35.	60.0	65.3	54.6	1.36E-01	1.98E-01	9.15E-02
55.	12.1	13.9	10.3	1.30E+02	1.43E+02	1.16E+02
55.	20.1	21.8	18.4	6.92E+00	1.01E+01	4.66E+00
55.	21.2	23.3	19.1	8.57E+00	1.08E+01	6.76E+00
55.	27.3	29.1	25.4	1.60E+00	2.15E+00	1.18E+00
55.	36.6	39.7	33.4	1.87E-01	2.21E-01	1.54E-01
55.	43.9	47.0	40.8	1.96E-02	3.28E-02	1.11E-02
80.	12.6	14.9	10.3	1.13E+01	1.46E+01	8.89E+00
80.	15.9	18.3	13.4	2.39E+00	3.41E+00	1.65E+00
80.	22.0	24.8	19.1	2.39E-01	4.00E-01	1.36E-01
100.	10.3	12.9	7.7	5.77E+00	7.42E+00	4.46E+00
100.	12.0	14.9	9.0	1.19E+00	1.99E+00	6.77E-01
100.	14.0	17.8	10.3	9.85E-01	1.16E+00	8.13E-01
156.	12.4	18.8	6.0	5.46E-02	8.40E-02	3.45E-02

NITROGEN

Angle (deg)	Energy E (MeV/ nuc)	E+ (MeV/ nuc)	E- (MeV/ nuc)	Cross Section σ (μb/MeV-sr)	σ+ (μb/MeV-sr)	σ- (μb/MeV-sr)
10.	13.4	15.7	11.1	3.16E+02	5.06E+02	1.91E+02
10.	32.4	37.1	27.6	3.45E+01	4.12E+01	2.77E+01
10.	35.6	40.1	31.1	1.63E+01	2.22E+01	1.18E+01
10.	39.5	43.8	35.3	9.90E+00	1.52E+01	6.25E+00
10.	41.8	45.9	37.8	1.04E+01	1.55E+01	6.79E+00
10.	45.8	49.6	41.9	1.81E+01	2.54E+01	1.27E+01
10.	59.2	62.7	55.8	1.50E+01	2.23E+01	9.79E+00
10.	72.3	75.5	69.1	1.86E+01	2.77E+01	1.21E+01
10.	77.7	80.8	74.7	1.53E+01	2.45E+01	9.24E+00
10.	85.0	90.2	79.7	2.18E+01	2.90E+01	1.62E+01
10.	92.1	95.1	89.0	5.24E+01	6.79E+01	4 02E+01
10.	95.2	98.2	92.2	5.07E+01	6.57E+01	3.89E+01
10.	105.9	113.3	98.4	8.29E+00	1.28E+01	5.24E+00
10.	122.7	126.1	119.2	4.21E+00	5.90E+00	2.96E+00
10.	136.8	133.8	127.8	3.35E+00	5.62E+00	1.90E+00
16.	13.3	15.4	11.1	3.23E+02	3.90E+02	2.76E+02
16.	23.6	27.9	19.2	4.09E+01	5.34E+01	3.11E+01
16.	29.9	32.1	27.6	2.62E+01	3.37E+01	2.02E+01
16.	40.2	42.1	38.2	1.47E+01	2.03E+01	1.05E+01
16.	49.9	53.3	46.5	5.74E+00	7.38E+00	4.43E+00
16.	60.8	65.8	55.8	5.52E+00	6.50E+00	4.54E+00
16.	74.8	80.4	69.1	5.10E+00	6.86E+00	3.75E+00

Angle (deg)	Energy E (MeV/ nuc)	E+ (MeV/ nuc)	E- (MeV/ nuc)	Cross Section σ (μb/MeV-sr)	σ+ (μb/MeV-sr)	σ- (μb/MeV-sr)
16.	89.6	95.0	84.1	1.79E+00	2.12E+00	1.46E+00
16.	97.6	100.4	94.7	1.95E+00	2.62E+00	1.44E+00
16.	104.3	107.1	101.5	1.44E+00	2.02E+00	1.01E+00
16.	112.9	115.7	110.1	3.33E-01	6.56E-01	1.52E-01
24.	13.2	15.2	11.1	2.94E+02	3.10E+02	2.59E+02
24.	24.4	25.9	23.0	2.32E+01	4.58E+01	1.06E+01
24.	29.7	31.8	27.6	1.24E+01	1.68E+01	8.98E+00
24.	55.6	58.6	52.6	5.91E-01	7.54E-01	4.60E-01
24.	62.4	65.3	59.5	4.38E-01	6.74E-01	2.76E-01
24.	68.6	71.5	65.8	4.23E-01	5.83E-01	3.02E-01
24.	80.0	85.4	74.6	8.01E-02	1.43E-01	4.18E-02
35.	13.0	15.0	11.1	2.46E+02	3.22E+02	1.87E+02
35.	22.2	23.6	20.8	2.56E+01	3.95E+01	1.62E+01
35.	29.6	31.5	27.6	3.19E+00	4.30E+00	2.35E+00
55.	13.1	15.1	11.1	4.34E+01	4.94E+01	3.73E+01
55.	21.9	23.7	20.0	3.91E+00	6.02E+00	2.47E+00
55.	23.1	25.4	20.8	1.82E+00	2.72E+00	1.19E+00
80.	13.7	16.2	11.1	2.10E+00	3.34E+00	1.27E+00

OXYGEN

Angle (deg)	Energy E (MeV/ nuc)	E+ (MeV/ nuc)	E- (MeV/ nuc)	Cross Section σ (μb/MeV-sr)	σ+ (μb/MeV-sr)	σ- (μb/MeV-sr)
10.	14.4	16.9	11.9	1.71E+02	3.07E+02	8.93E+01
10.	23.7	26.8	20.6	3.70E+01	6.20E+01	2.10E+01
10.	28.9	34.7	23.2	1.02E+01	1.28E+01	8.16E+00
10.	34.8	40.0	29.7	1.06E+01	1.32E+01	8.44E+00
10.	38.3	43.2	33.5	5.05E+00	6.97E+00	3.62E+00
10.	42.6	47.1	38.0	6.09E+00	8.29E+00	4.42E+00
10.	47.1	53.5	40.6	5.71E+00	6.85E+00	4.57E+00
10.	54.0	58.0	50.0	6.17E+00	8.98E+00	4.15E+00
10.	66.4	72.7	60.0	8.06E+00	1.01E+01	6.42E+00
10.	77.9	81.4	74.4	1.75E+01	2.18E+01	1.39E+01
10.	83.7	87.1	80.3	2.20E+01	2.61E+01	1.78E+01
10.	89.2	92.6	85.9	2.34E+01	2.80E+01	1.88E+01
10.	93.9	97.2	90.6	2.85E+01	3.34E+01	2.36E+01
10.	99.2	102.5	96.0	3.67E+01	4.25E+01	3.10E+01
10.	102.6	105.9	99.3	3.04E+01	3.56E+01	2.52E+01
10.	109.3	112.6	106.1	1.75E+01	2.29E+01	1.33E+01
10.	116.1	122.0	110.2	4.15E+00	7.93E+00	2.62E+00
16.	14.3	16.6	11.9	1.35E+02	1.76E+02	1.02E+02
16.	23.5	26.4	20.6	2.14E+01	2.81E+01	1.61E+01
16.	27.4	30.0	24.7	1.25E+01	1.86E+01	8.15E+00
16.	48.9	52.8	45.0	1.89E+00	2.42E+00	1.47E+00
16.	53.7	57.5	50.0	1.26E+00	1.72E+00	9.14E-01

Angle (deg)	Energy E (MeV/ nuc)	E+ (MeV/ nuc)	E- (MeV/ nuc)	Cross Section σ (μb/MeV-sr)	σ+ (μb/MeV-sr)	σ- (μb/MeV-sr)
16.	66.8	73.5	60.0	1.53E+00	1.92E+00	1.21E+00
16.	77.7	80.9	74.4	1.40E+00	1.96E+00	9.89E-01
16.	88.7	91.9	85.6	5.83E-01	1.04E+00	3.04E-01
16.	99.1	102.4	95.7	3.03E-01	4.84E-01	1.83E-01
16.	102.3	106.2	99.3	1.72E-01	3.08E-01	8.98E-02
16.	107.3	111.5	103.1	1.29E-01	2.16E-01	7.33E-02
24.	14.1	16.3	11.9	9.03E+01	1.03E+02	7.74E+01
35.	14.0	16.1	11.9	8.23E+01	1.27E+02	5.20E+01
55.	14.1	16.2	11.9	1.10E+01	1.45E+01	8.30E+00

FLUORINE

Angle (deg)	Energy E (MeV/ nuc)	E+ (MeV/ nuc)	E- (MeV/ nuc)	Cross Section σ (μb/MeV-sr)	σ+ (μb/MeV-sr)	σ- (μb/MeV-sr)
10.	24.5	27.7	21.3	1.04E+01	2.04E+01	4.73E+00
10.	29.9	35.9	23.9	3.39E+00	4.42E+00	2.57E+00
10.	36.0	41.4	30.7	1.45E+00	2.23E+00	9.14E-01
10.	39.7	44.7	34.6	9.86E-01	1.65E+00	5.60E-01
10.	45.3	51.2	39.3	1.56E+00	2.08E+00	1.16E+00
10.	53.4	60.1	46.6	1.76E+00	2.40E+00	1.28E+00
10.	68.8	75.3	62.2	2.04E+00	2.78E+00	1.48E+00
10.	80.7	84.4	77.1	7.83E+00	9.82E+00	6.21E+00
10.	86.7	90.3	83.2	7.70E+00	9.78E+00	6.04E+00
10.	92.4	95.9	89.0	9.23E+00	1.16E+01	7.28E+00
10.	97.3	100.8	93.9	5.49E+00	7.39E+00	4.04E+00
10.	104.6	109.8	99.4	3.97E+00	5.50E+00	3.07E+00
10.	118.3	126.5	110.0	6.44E-01	1.15E+00	3.36E-01
16.	24.3	27.3	21.3	4.99E+00	7.45E+00	3.26E+00
16.	50.7	54.7	46.6	2.65E-01	4.24E-01	1.60E-01
16.	60.1	69.4	51.7	1.48E-01	2.36E-01	8.93E-02

NEON

Angle (deg)	Energy E (MeV/ nuc)	E+ (MeV/ nuc)	E- (MeV/ nuc)	Cross Section σ (μb/MeV-sr)	σ+ (μb/MeV-sr)	σ- (μb/MeV-sr)
10.	32.7	39.3	26.1	7.85E-01	1.25E+00	4.74E-01
10.	49.5	56.0	42.9	7.78E-01	1.11E+00	5.37E-01
10.	63.7	76.5	50.9	3.22E-01	5.40E-01	1.83E-01
10.	88.3	92.3	84.3	1.67E+00	2.58E+00	1.06E+00
10.	94.9	98.9	91.0	1.77E+00	2.72E+00	1.12E+00
10.	101.1	105.0	97.3	1.86E+00	2.86E+00	1.17E+00
10.	106.5	110.3	102.7	2.77E+00	3.95E+00	1.90E+00
10.	112.6	116.4	108.9	1.44E+00	2.42E+00	8.20E-01
10.	120.3	127.8	112.7	3.03E-01	7.02E-01	1.07E-01
16.	26.5	29.8	23.2	2.11E+00	3.55E+00	1.20E+00

Table 4

Fitted Parameters Using a Thermal Model for Central Collision Data

Element	σ_1 (μb)	β_1	τ_1 (MeV)	σ_2 (μb)	β_2	τ_2 (MeV)	Applicable Energy Regime
Boron	389000	.0696	23.2	75200	.146	36.6	16°:<30 MeV/nuc; 24°:<40 MeV/nuc; 35°:<30 MeV/nuc; 55° to 125°
Carbon	382000	.0746	28.2	33300	.170	39.4	16°:<30 MeV/nuc; 24°:<40 MeV/nuc; 35° to 100°
Nitrogen	287000	.0834	32.1	5980	.215	42.8	10°:<45 MeV/nuc; 16°:<50 MeV/nuc; 24°:<65 MeV/nuc; 35° to 80°

Table 5

Fitted Parameters Using a Thermal Model for Peripheral Collision Data

Element	σ_1 (μb)	β_1	τ_1 (MeV)	T_1 (MeV)	σ_2 (μb)	β_2	τ_2 (MeV)	Applicable Energy Regime
Boron	6.84×10^8	.424	5.4	9	13600	.288	41.6	16°:>40 MeV/nuc; 24°:>40 MeV/nuc
Carbon	44300	.402	16.4	23.4	7060	.276	45	16°:>50 MeV/nuc; 24°:>50 MeV/nuc
Nitrogen	4110	.416	20.6	31.7	2760	.328	41.8	10°:>45 MeV/nuc; 16°:>45 MeV/nuc
Oxygen	12500	.424	15	25	1200	.338	34.8	10°:>40 MeV/nuc; 16°:>40 MeV/nuc

Table 6

Fireball Temperature, Velocity, and Number of Participants as a Function of Impact Parameter for Carbon Production

Impact parameter b/b_{max}	Fireball temperature (MeV)	Fireball velocity (V/c)	Participants
.1	9.2	.131	140
.2	9.3	.133	138
.3	9.7	.139	133
.4	10.5	.150	122
.5	11.3	.161	104
.6	12.2	.167.	81
.7	13.9	.179	55
.8	17.5	.185	34
.9	39.4	.191	16

Figure Captions

Figure 1. Drawing of the positions of the Lexan detectors and uranium target in the vacuum chamber.

Figure 2. Drawing of two etched particle tracks for the last three Lexan sheets at the end of range of the particle. The particle on the left would be detected in this experiment by the hole in the middle sheet. H is the sheet thickness before etching. ΔX is the track length in the last sheet after etching. $\bar{R}$ is the distance from the center of the cone to the point where the particle stopped. Particle on the right would not be detected.

Figure 3. Plot of the etch rate V_T^* vs average range $\bar{R}$ for 400 events from the 3 day UV on each side and 30-hour etch.

Figure 4. Histograms for number of events vs range-adjusted etch rate V_T(@100 μ).

a) Three day UV on each side and 30-hour etch.

b) One day UV on each side and 30-hour etch.

Figure 5. Plot of boron data from 16° to 125°.

Figure 6. Plot of carbon data from 10° to 100°.

Figure 7. Plot of nitrogen data.

Figure 8. Plot of oxygen data.

Figure 9. Plot of fluorine data.

Figure 10. Plot of neon data.

Figure 11. Fit of two-source thermal model to the boron data.

Figure 12. Fit of two-source thermal model to the carbon data.

Figure 13. Fit of two-source thermal model to the nitrogen data.

Figure 14. Fits of a single source to oxygen projectile fragmentation.

a) Fit with a temperature of 8 MeV.

b) Fit with a temperature of 15 MeV.

Figure 15. a) Effect of using a thick target on the distribution of oxygen from projectile fragmentation.

b) Effect of multiple isotopes on the distribution of oxygen from projectile fragmentation.

Figure 16. Two-source thermal fits from projectile fragmentation.

a) Oxygen.

b) Nitrogen.

Figure 17. Two-source thermal fits to high-energy boron data.

a) Fit with source parameters $\tau_1 = 5.4$, $\tau_2 = 41.6$.

b) Fit with source parameters $\tau_1 = 11$, $\tau_2 = 43.2$.

Figure 18. Two-source thermal fit to high-energy carbon data.

Figure 19. Fit of a model of the fireball type to carbon data.

Figure 20. Plot of contour of constant invariant cross section ($\mu b/sr\text{-}MeV^2/c$) in transverse momentum $P_\perp$ vs longitudinal momentum $P_\parallel$ for boron fragments.

Figure 21. Plot of source velocity β_o vs fragment velocity in the moving frame β' for low energy B, C, and N.

Figure 22. Plot of invariant cross section vs momentum in the moving frame. Plotted points are from this experiment. The lines are from 400 MeV/nucleon Ne + U.

Figure 23. Histograms of projectile fragmentation with target pickup. Parallel distributions (z-direction) and trans-

verse component (x or y directions are shown). The projectile velocity is 0.43 c.

a) Fragmentation to mass 3.

b) Fragmentation to mass 16.

Figure 24. Histogram of projectile fragmentation with target pick-up to mass 3 for a projectile with velocity 0.204 c.

Figure 25. Histogram of projectile fragmentation to mass 16 with and without momentum constraints. There is no target contribution.

Figure 26. Histogram of projectile fragmentation to mass 16 with target pickup and a momentum constraint on the projectile nucleus. The projectile has a velocity of 0.43 c.

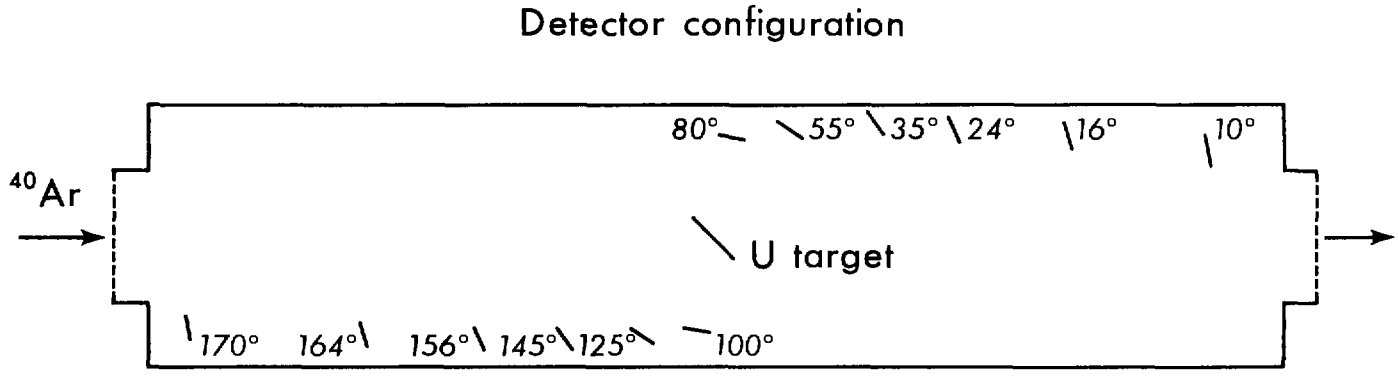

XBL 799-12012

FIGURE 1

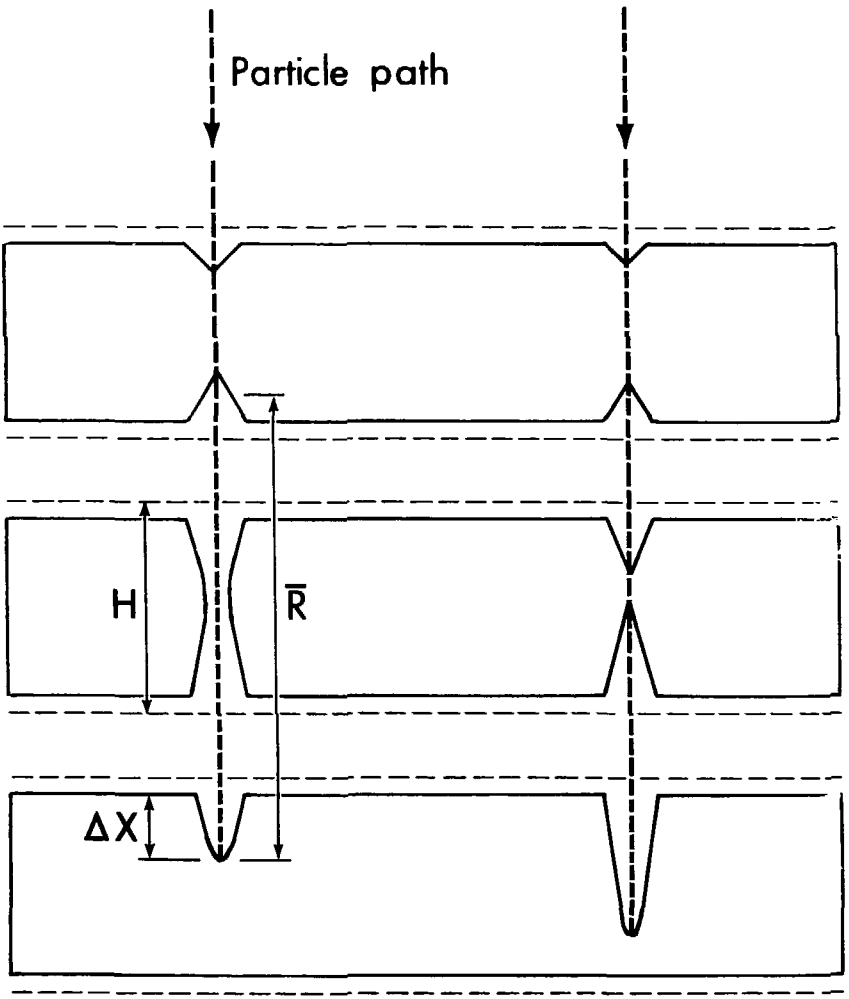

XBL 799-12013

FIGURE 2

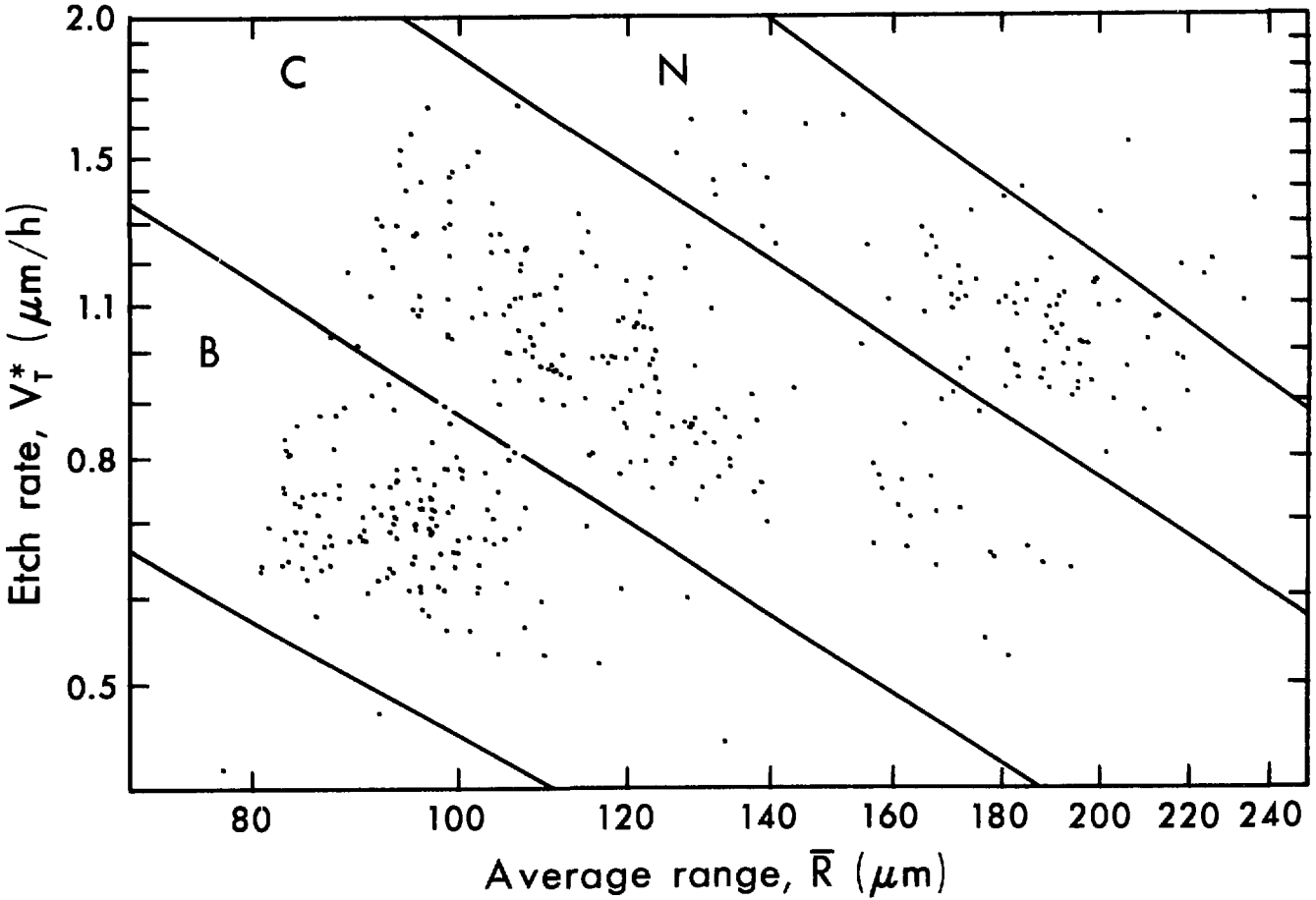

XBL 799-12009

FIGURE 3

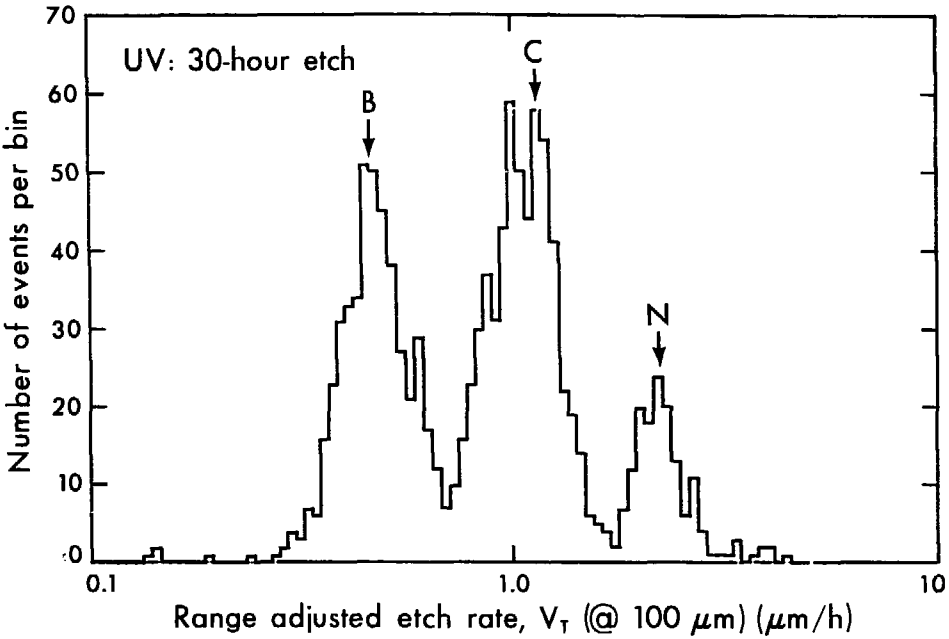

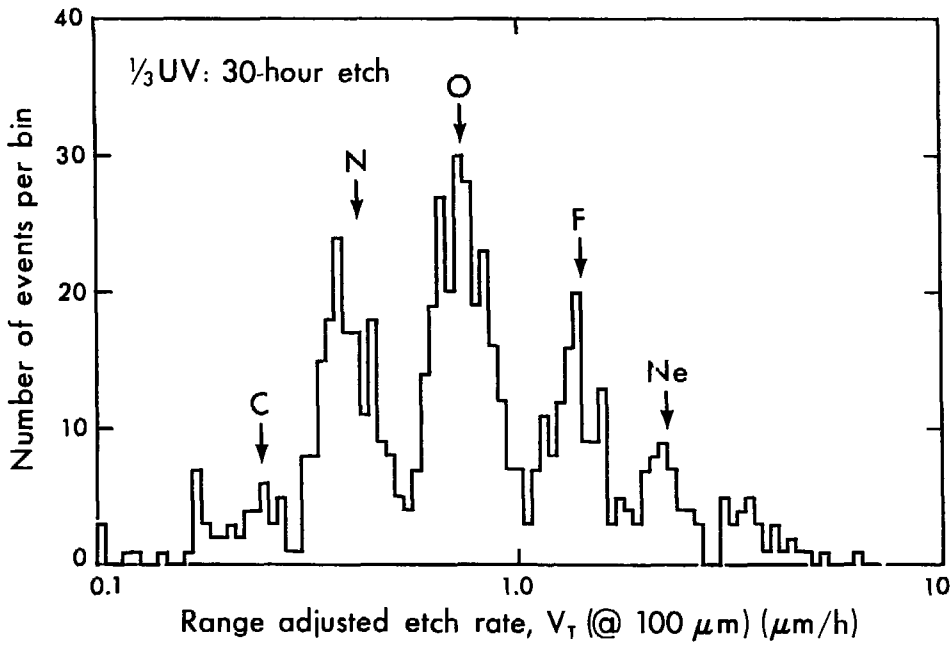

XBL 799-12014

FIGURE 4

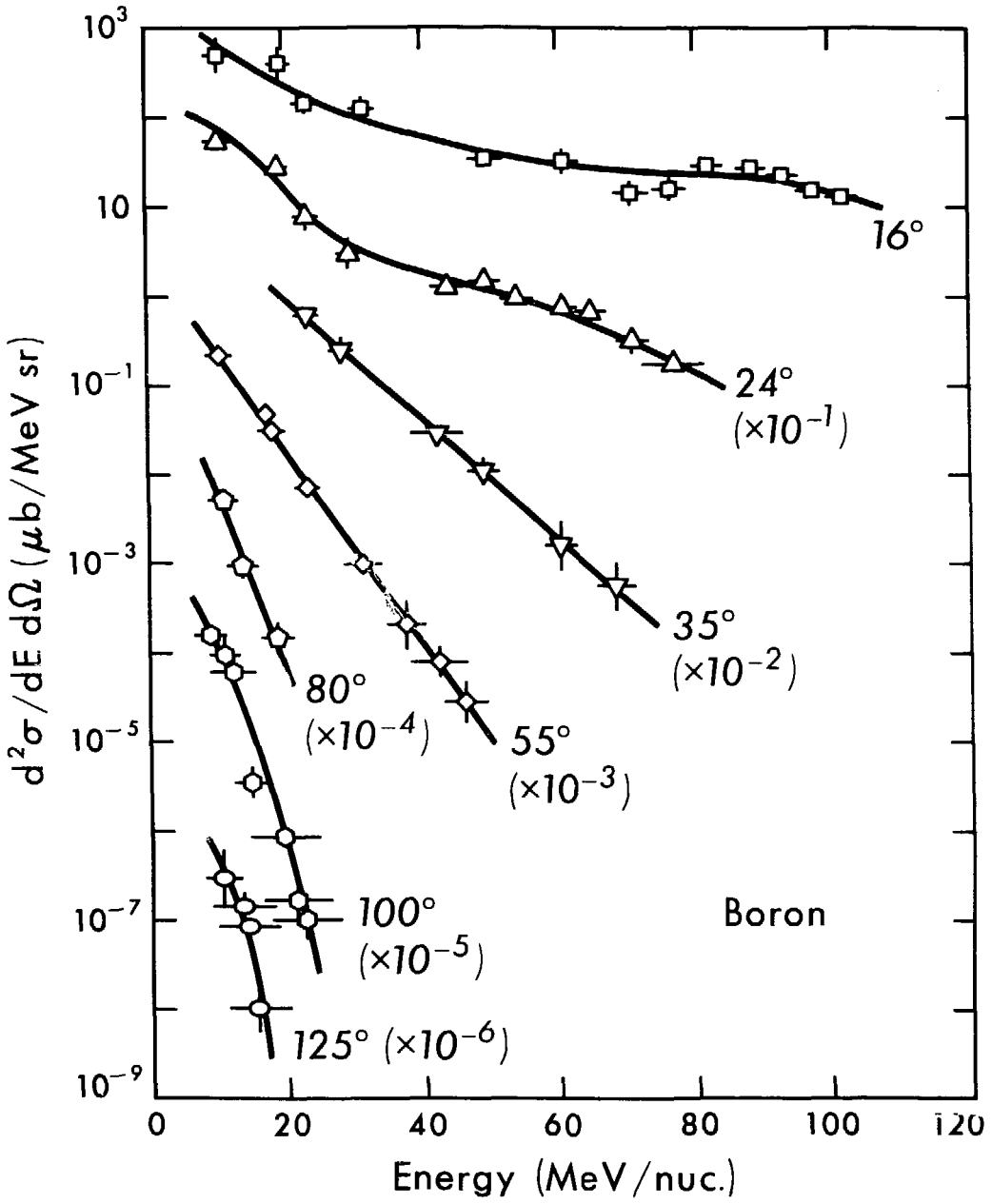

XBL 799-12015

FIGURE 5

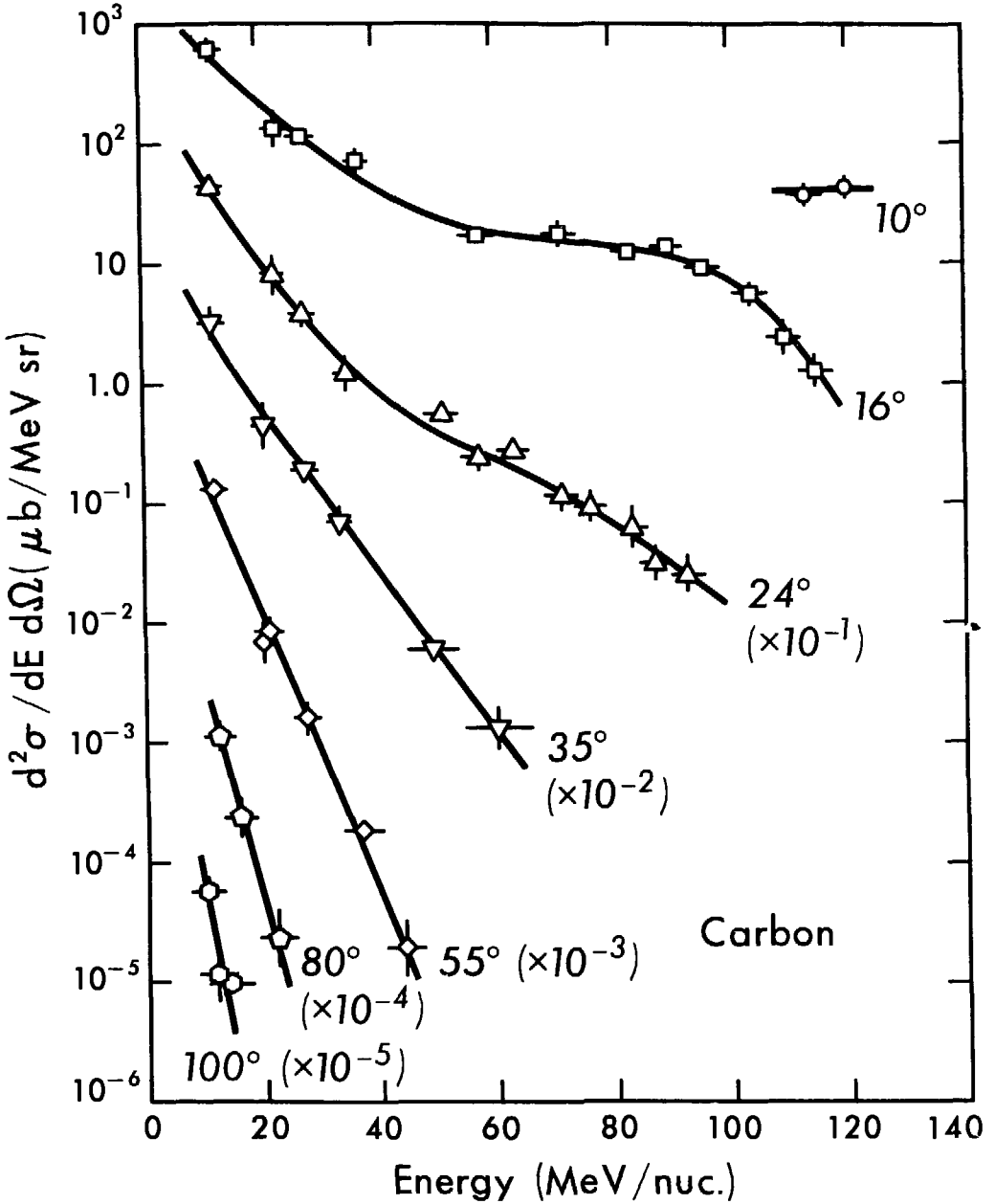

XBL 799-12016

FIGURE 6

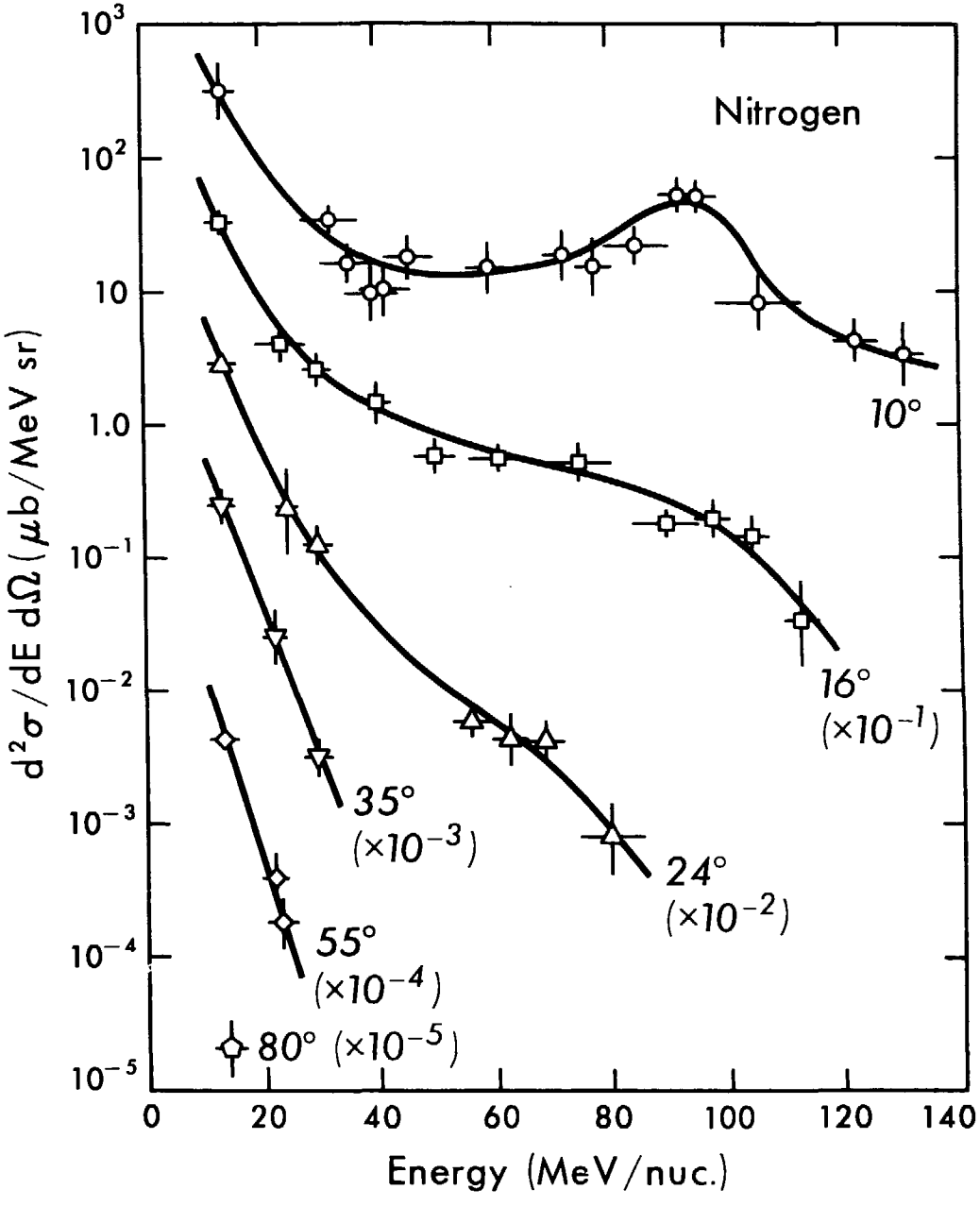

XBL 799-12017

FIGURE 7

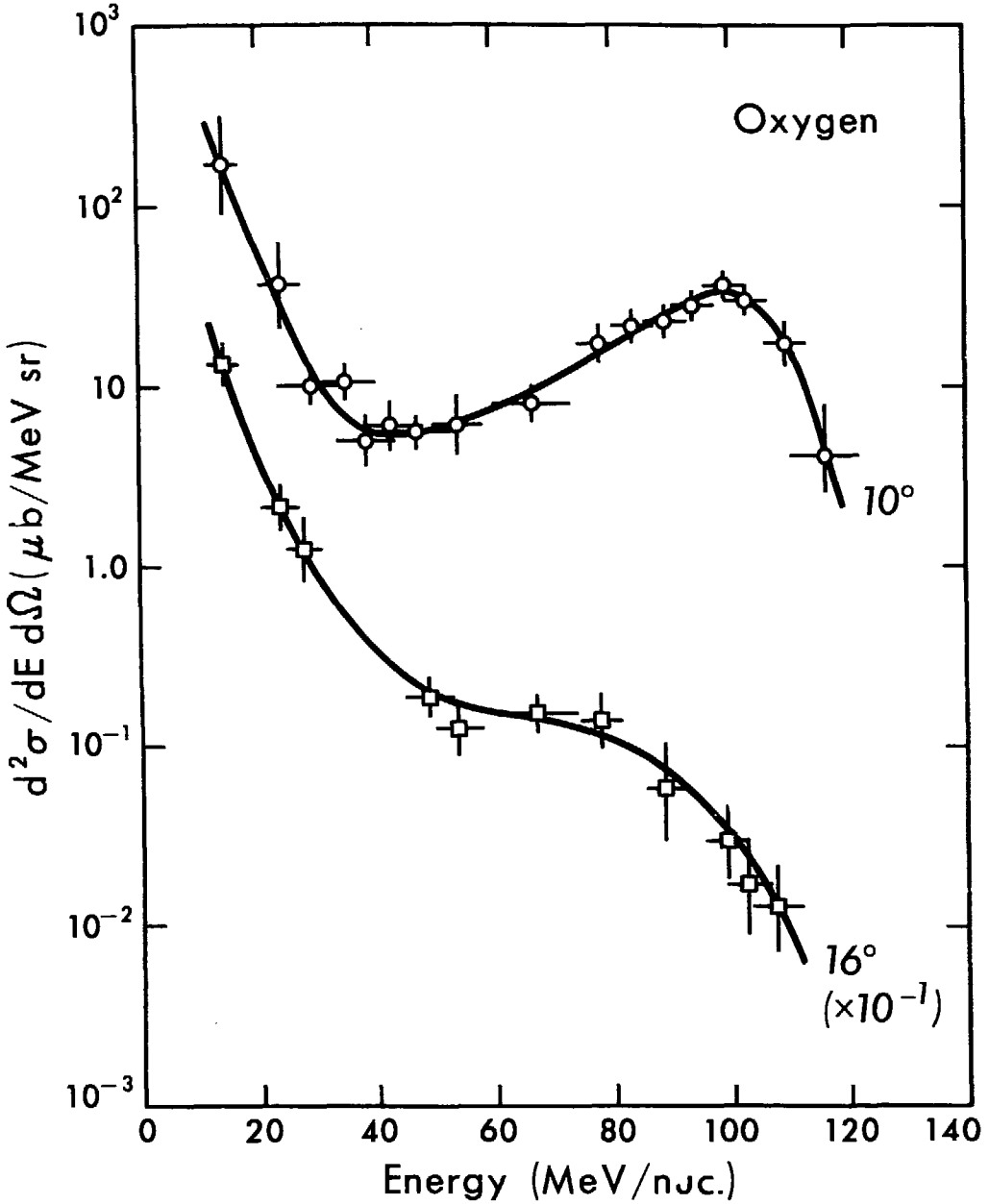

XBL 798-2477

FIGURE 8

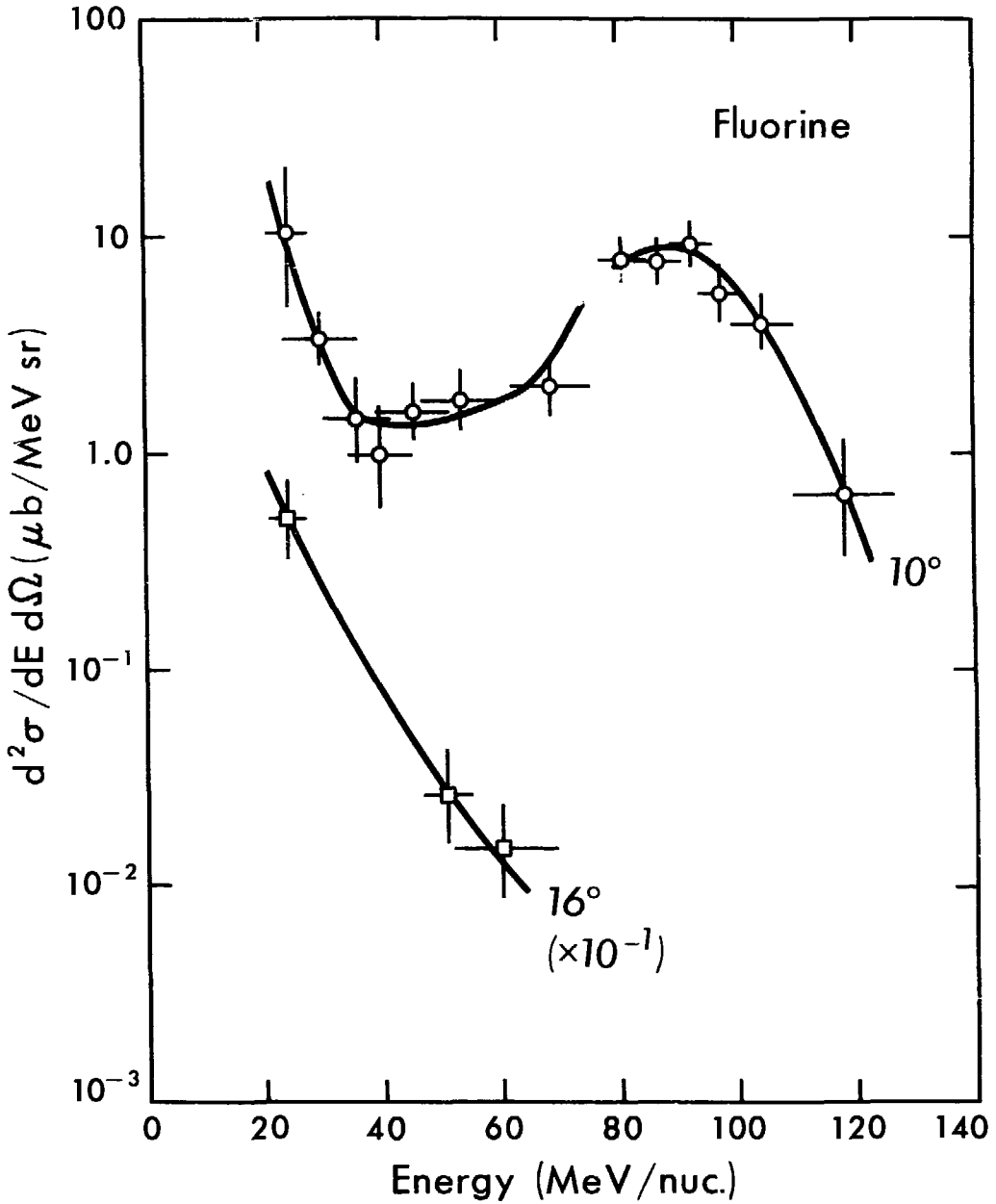

XBL 799-12018

FIGURE 9

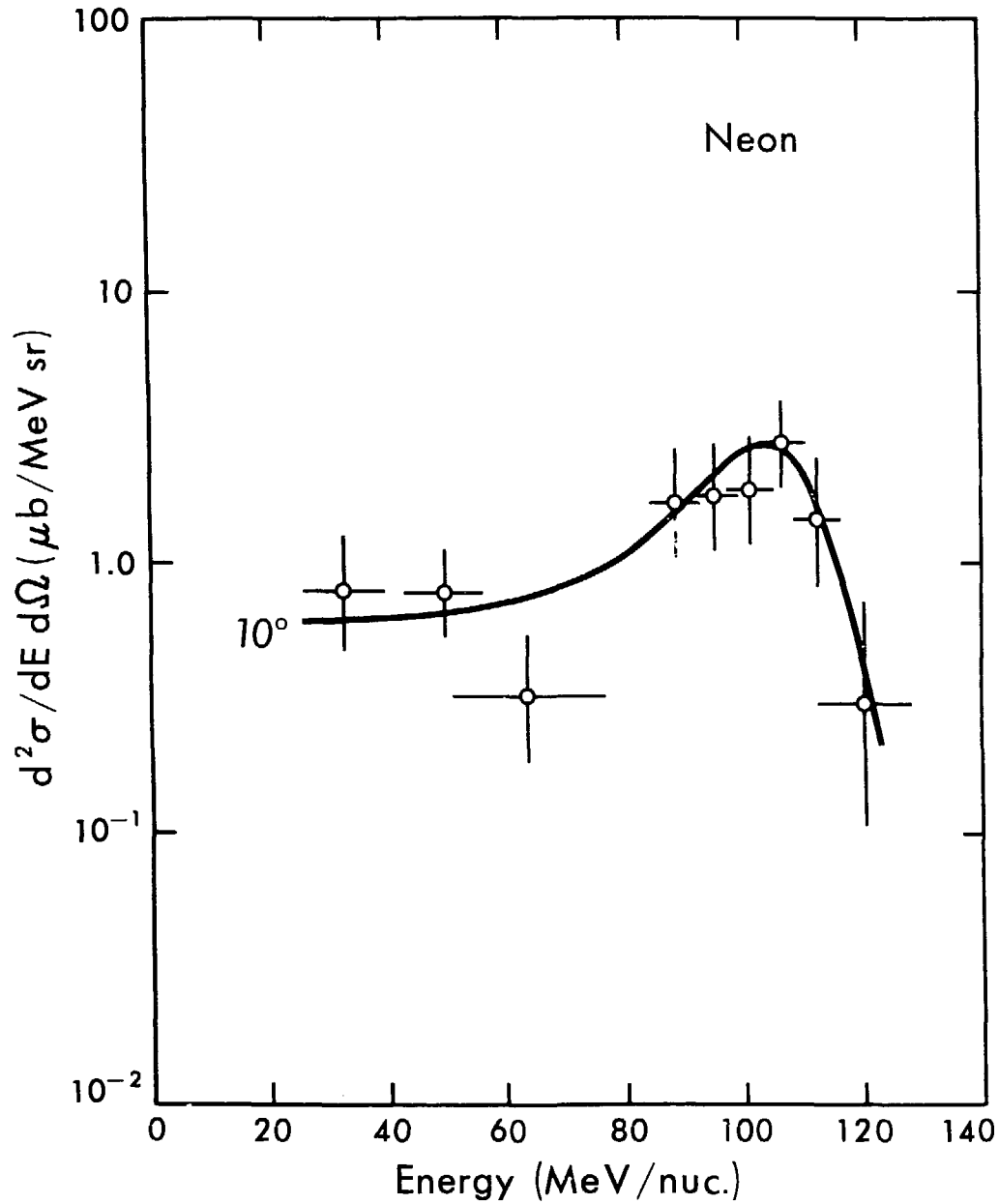

XBL 799-12019

FIGURE 10

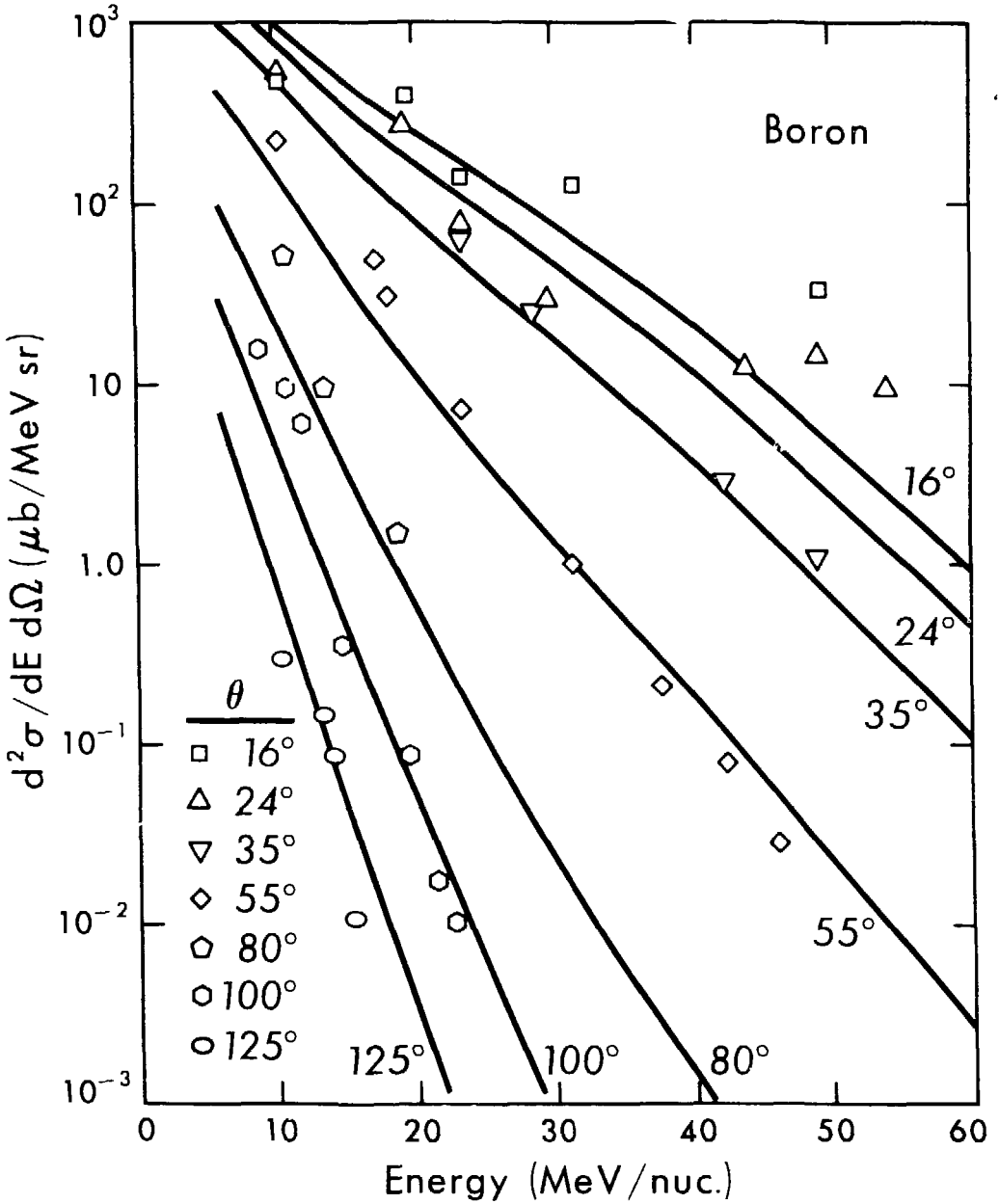

XBL 798-2476

FIGURE 11

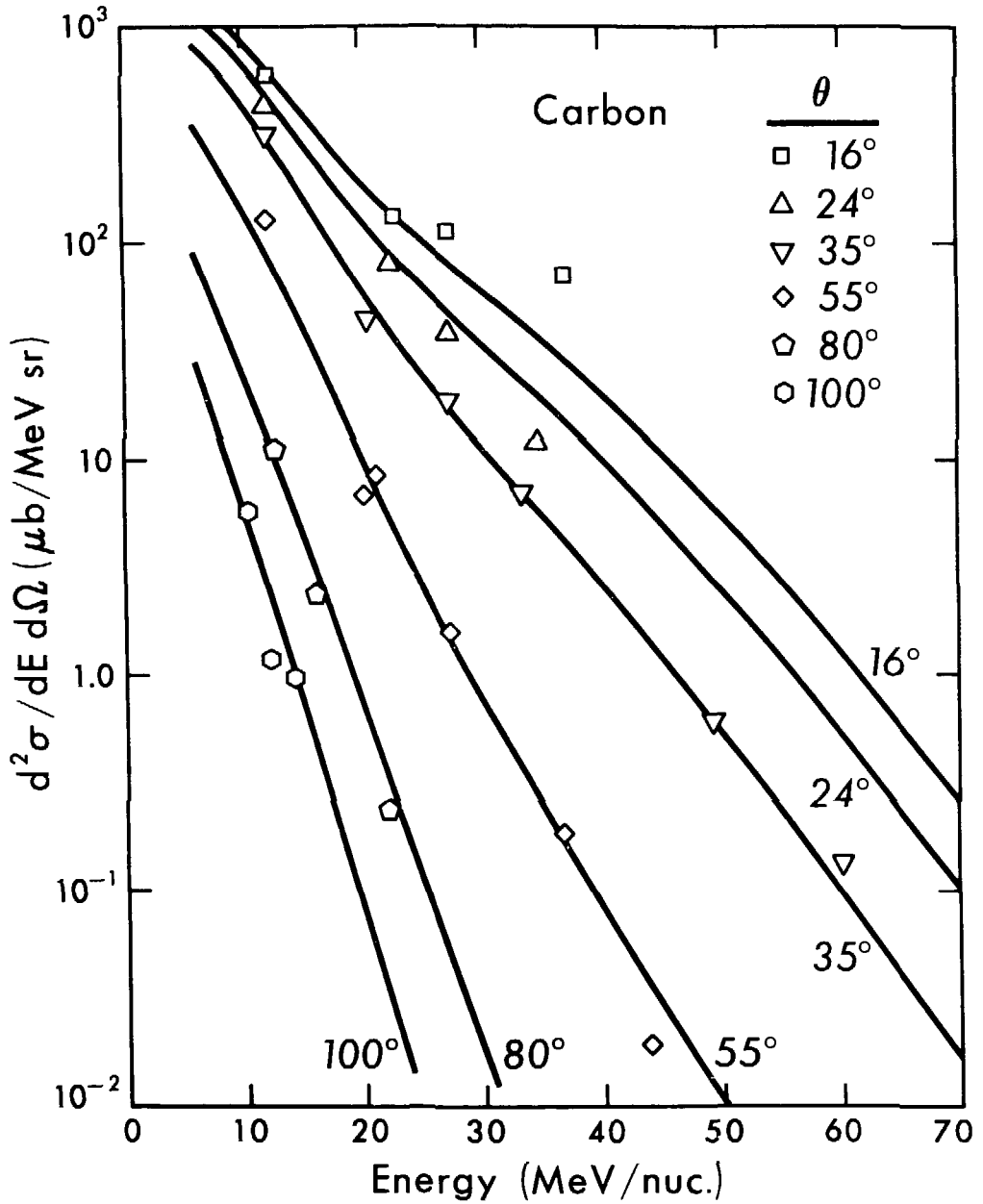

XBL 799-12020

FIGURE 12

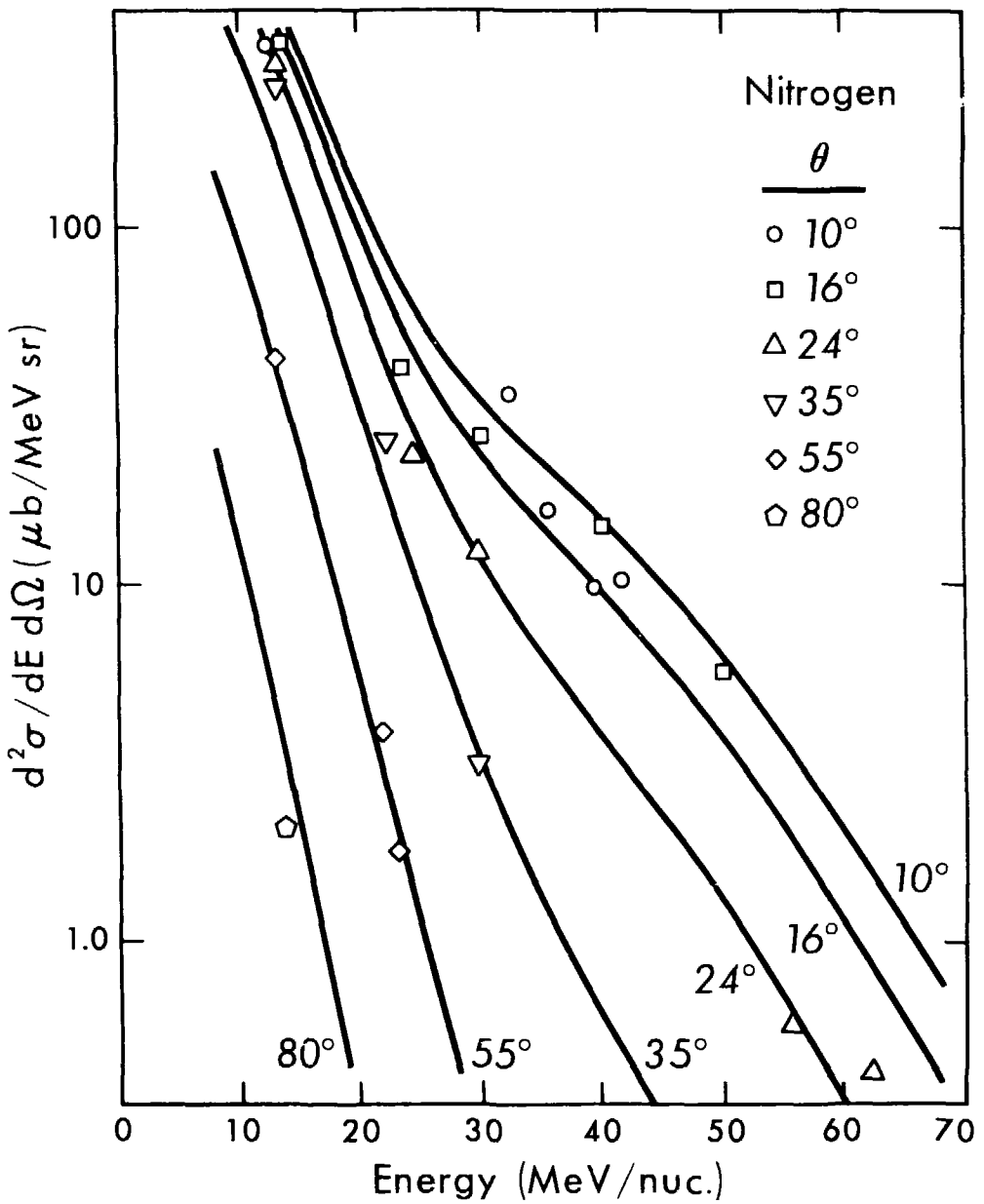

XBL 799-12021

FIGURE 13

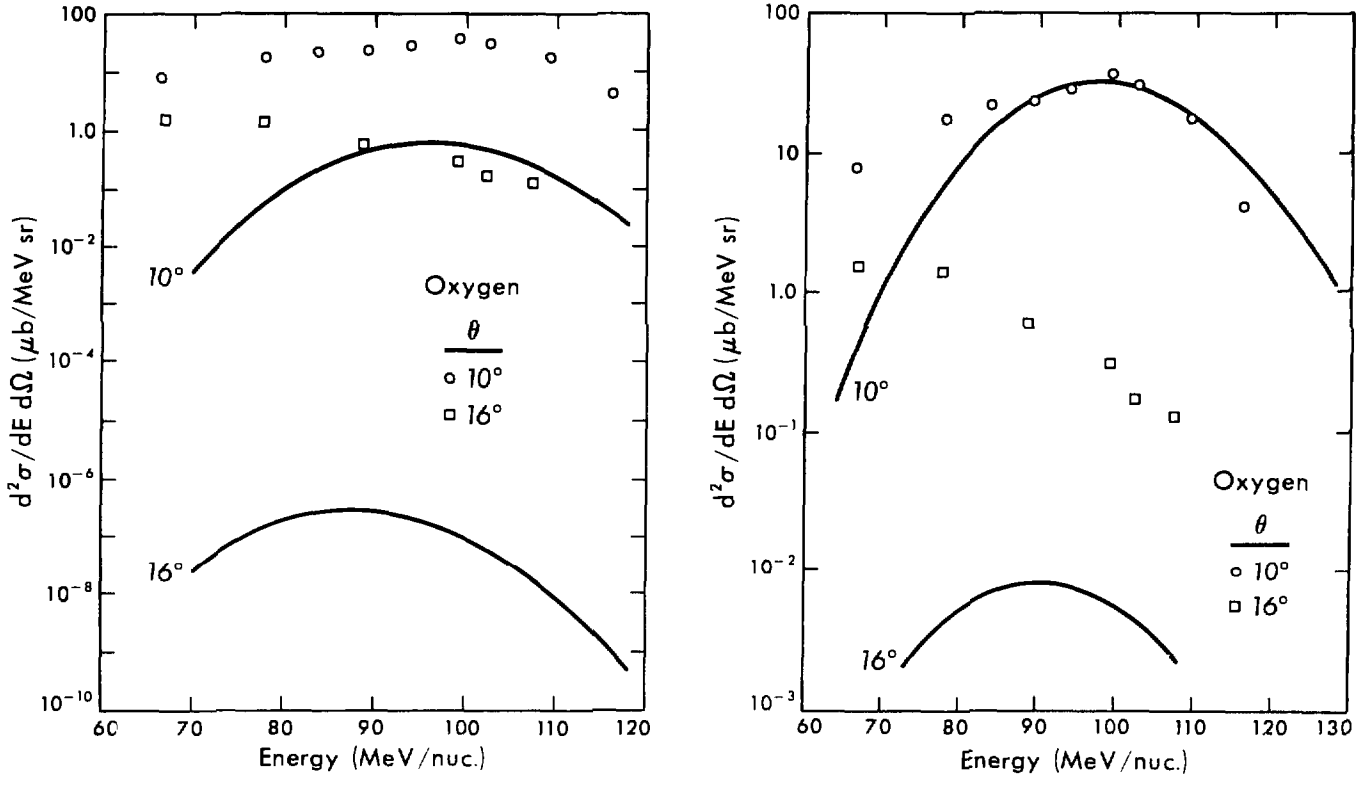

XBL 799-12022

FIGURE 14

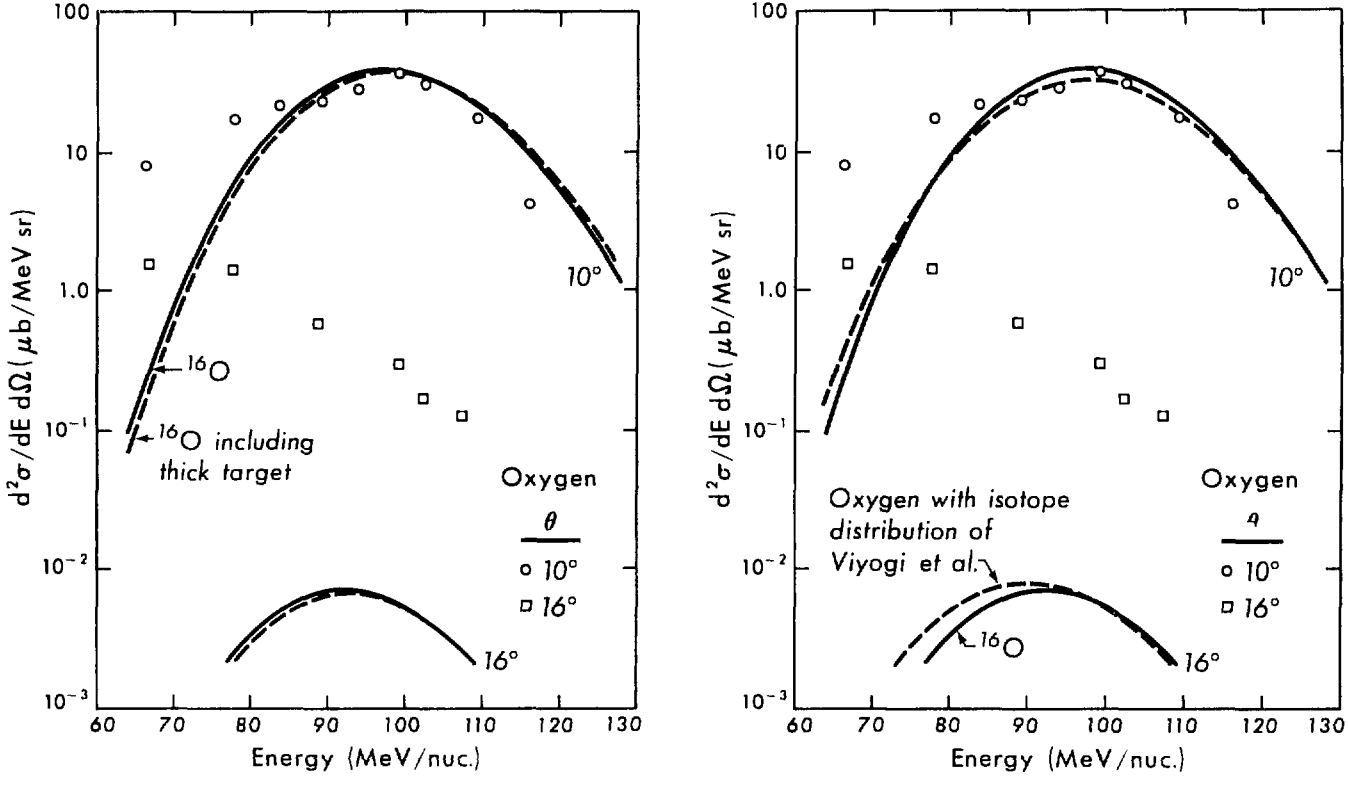
100
10
1.0
10^{-1}
10^{-2}
10^{-3}
$d^2\sigma/dE\,d\Omega$ (μb/MeV sr)
60 70 80 90 100 110 120 130
Energy (MeV/nuc.)
10°
16°
^{16}O
^{16}O including thick target
Oxygen
θ
o 10°
□ 16°
Oxygen with isotope distribution of Viyogi et al.
^{16}O
XBL 799-12023

FIGURE 15

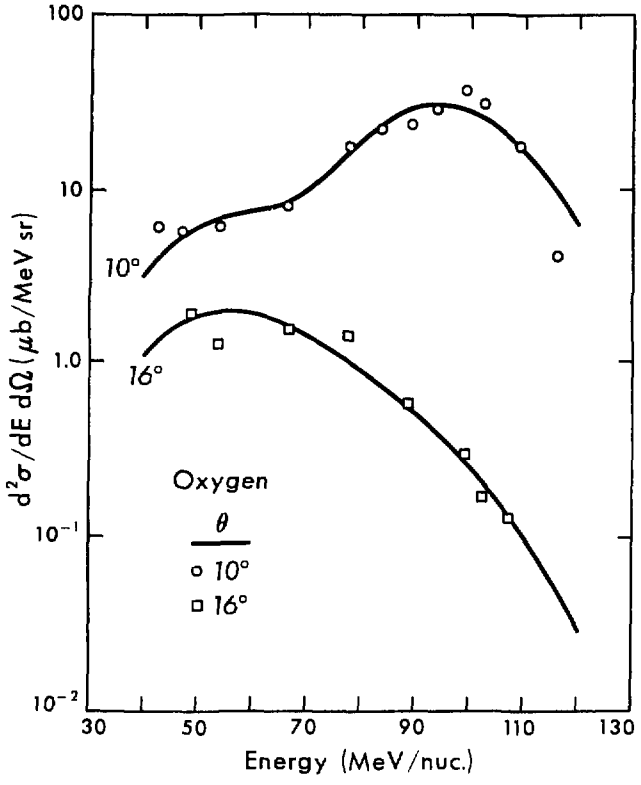

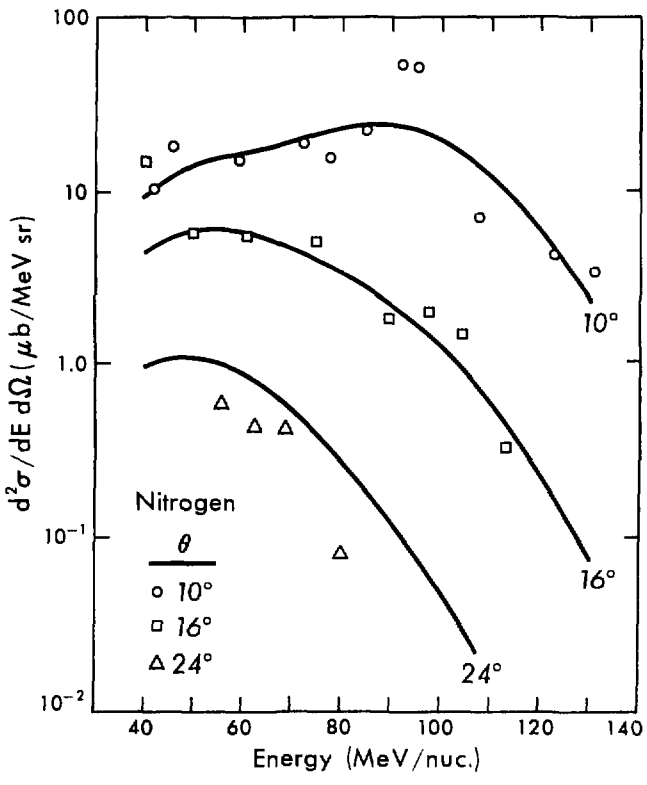

XBL 799-12024

FIGURE 16

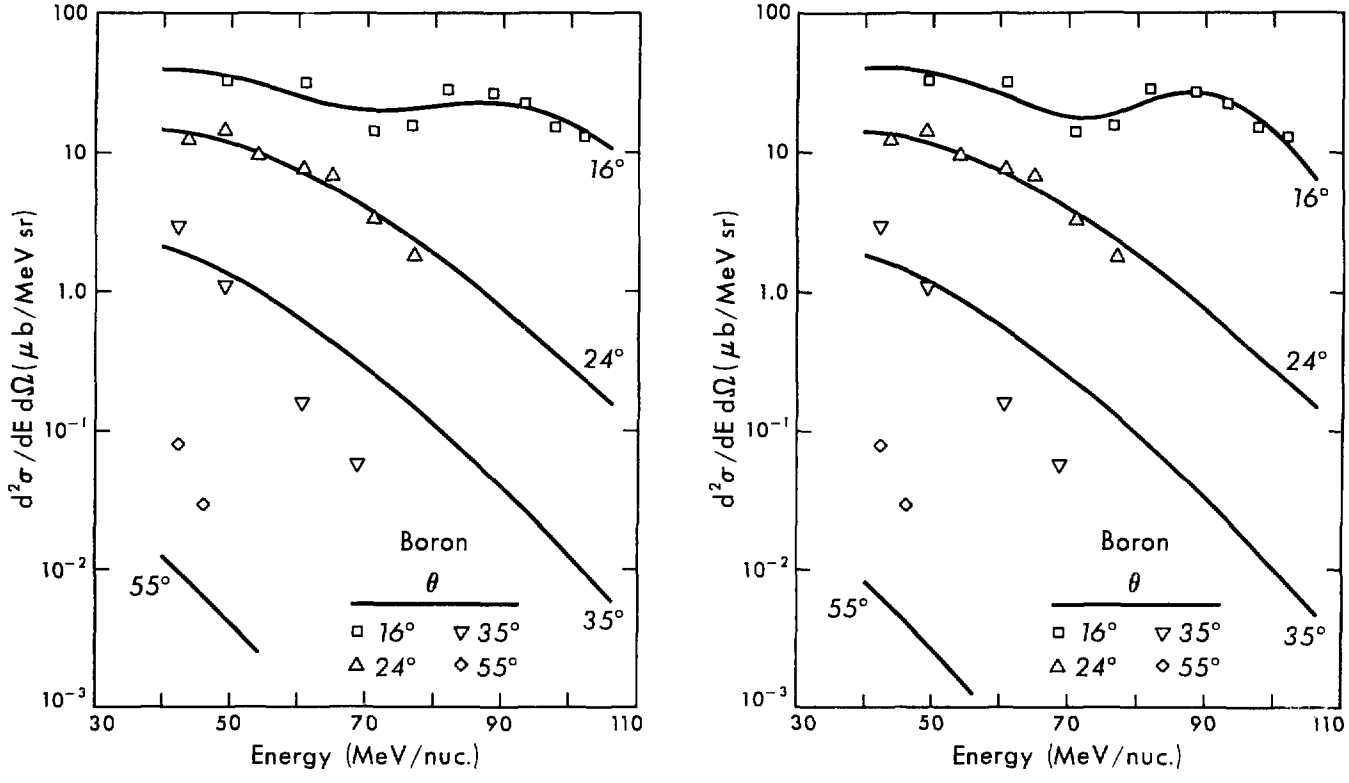

XBL 799-12025

FIGURE 17

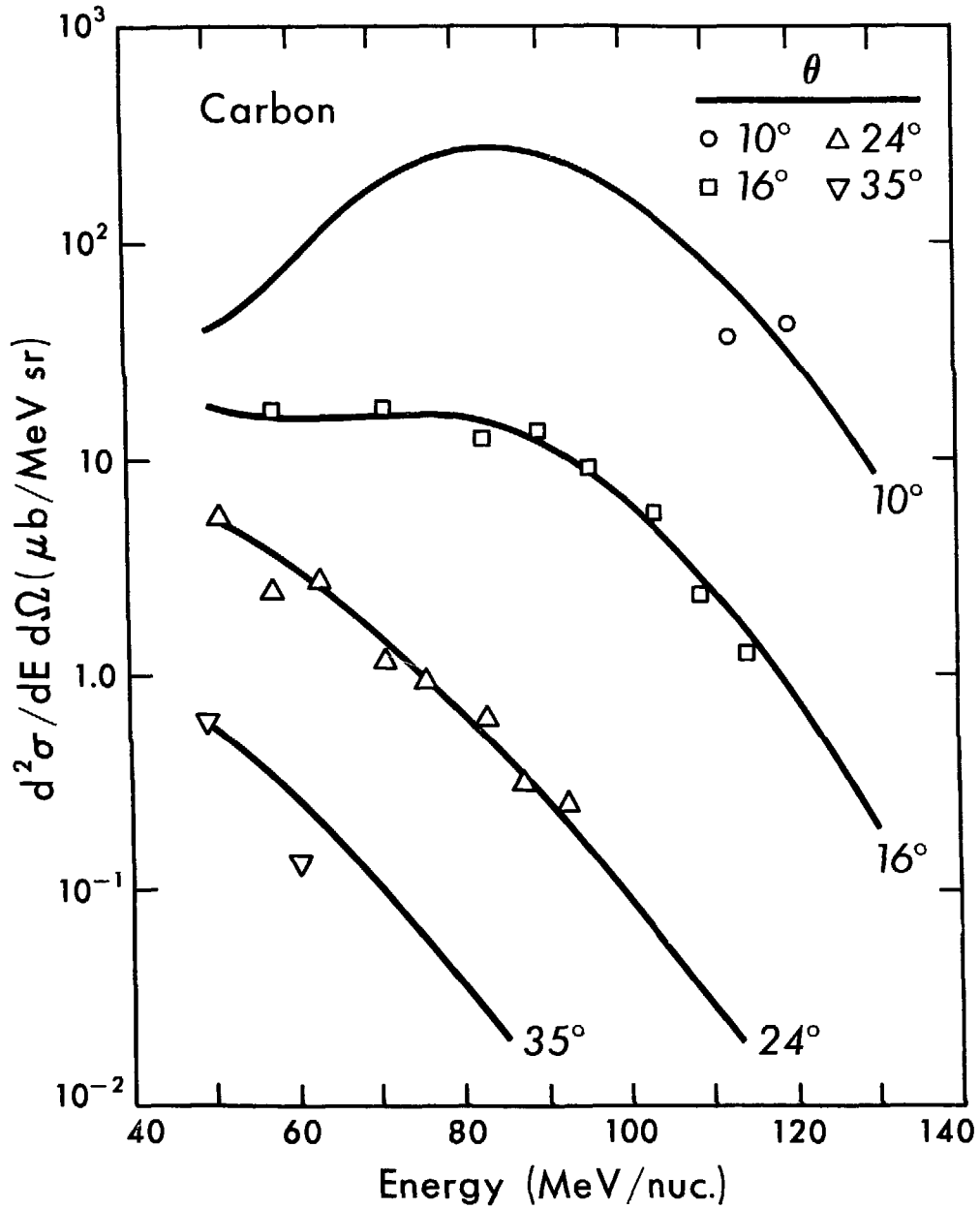

XBL 799-12027

FIGURE 13

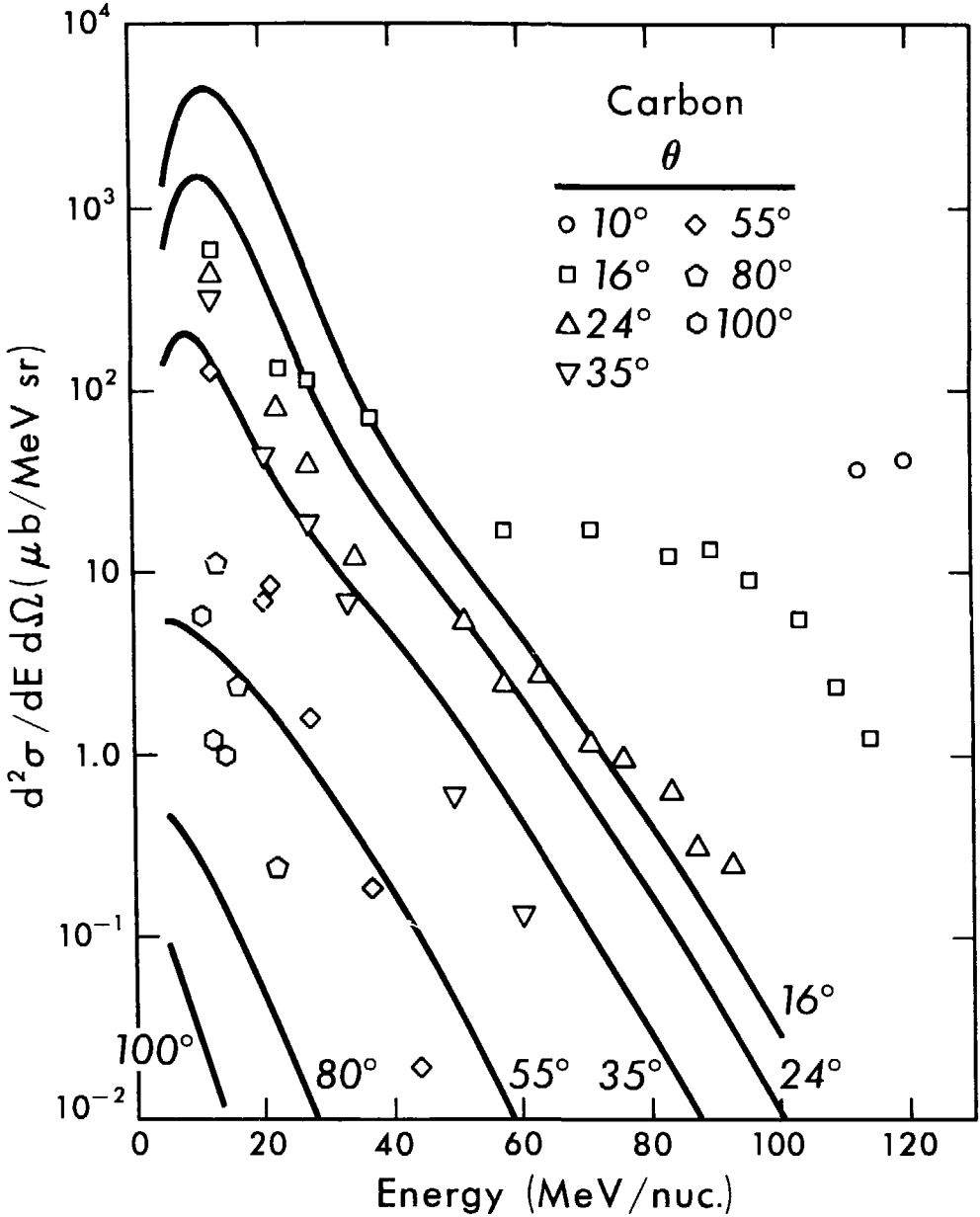

XBL 799-12028

FIGURE 19

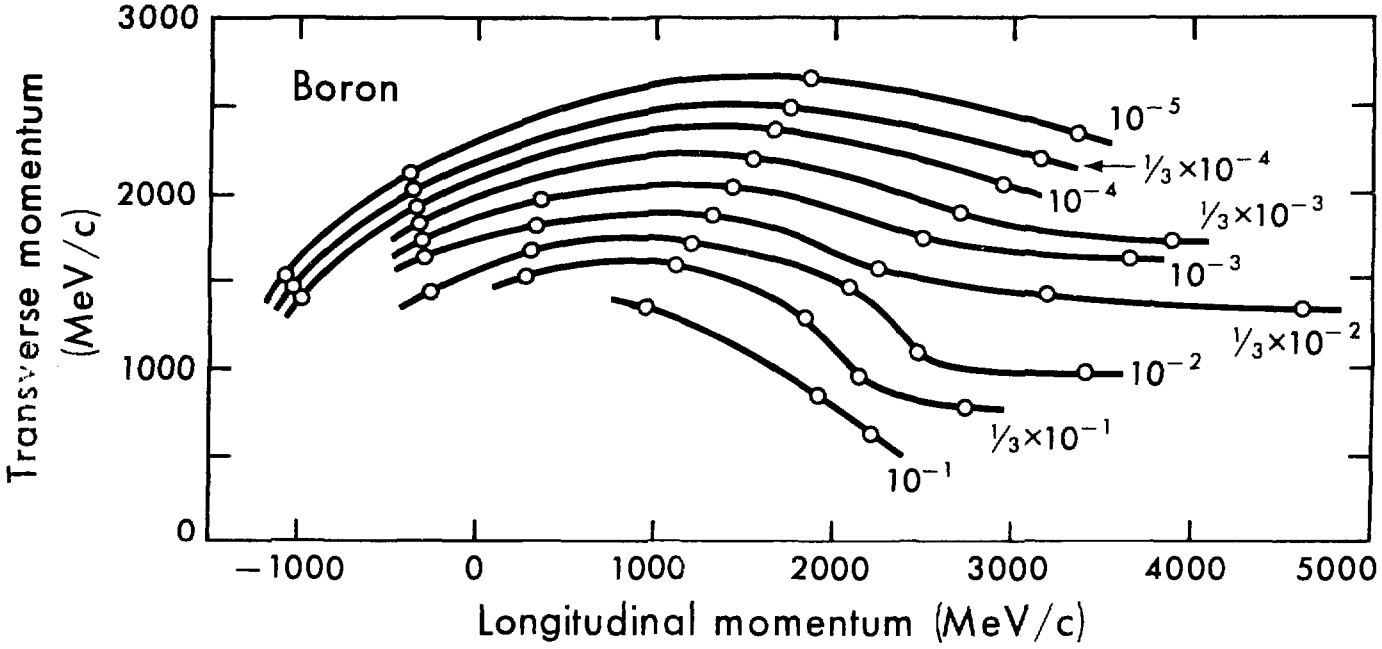

XBL 799-12030

FIGURE 20

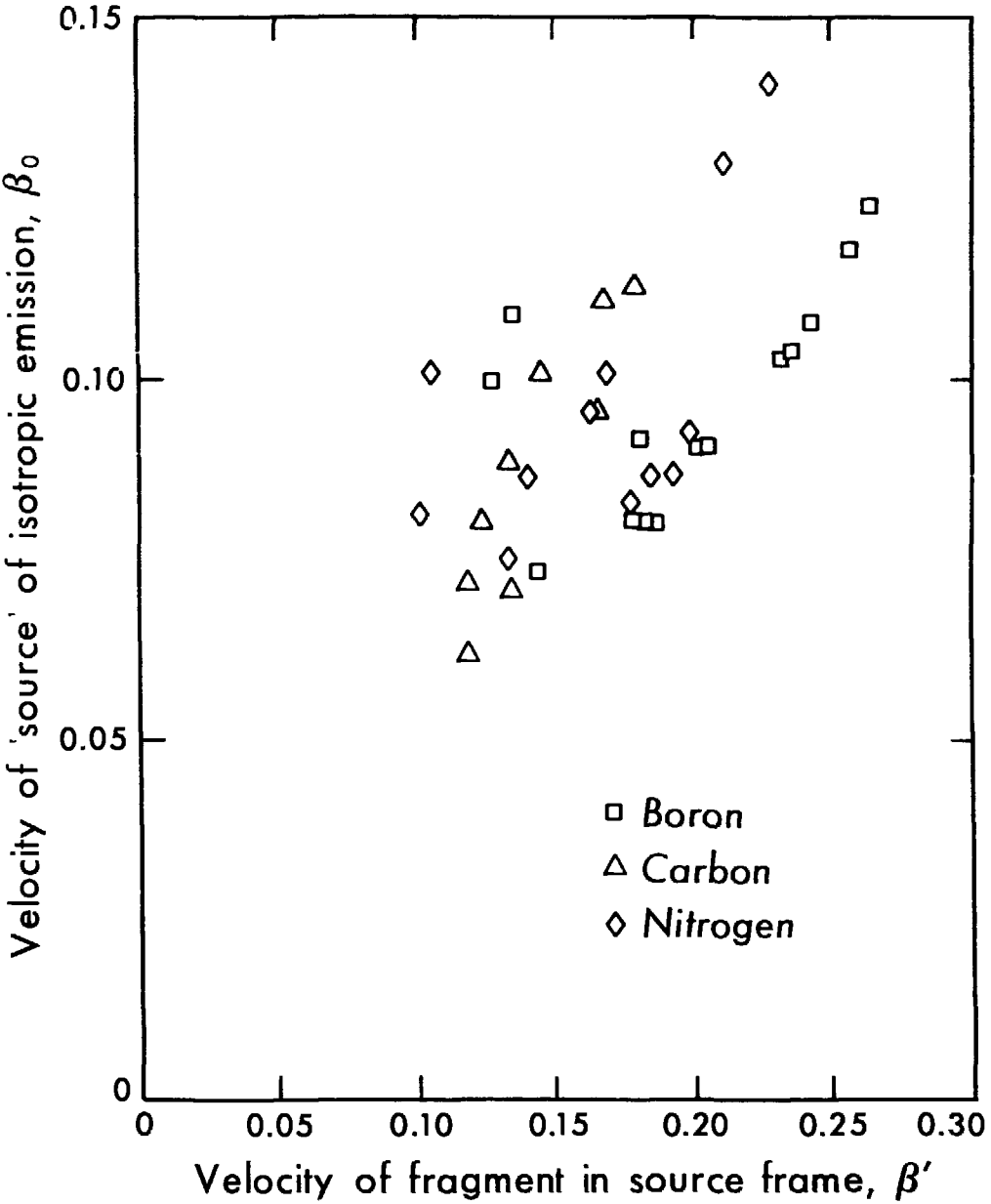

XBL 799-12029

FIGURE 21

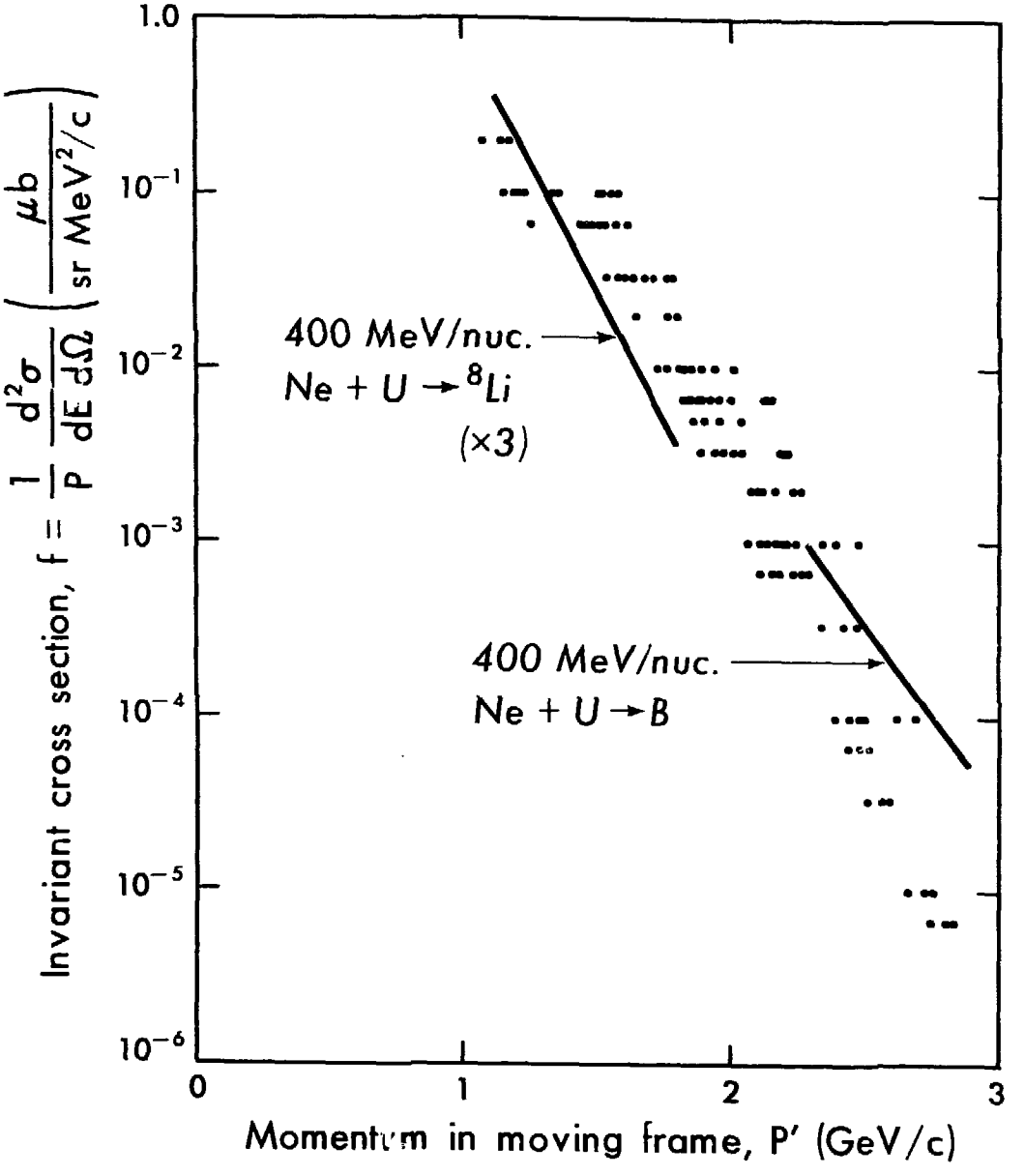

XBL 799-12032

FIGURE 22

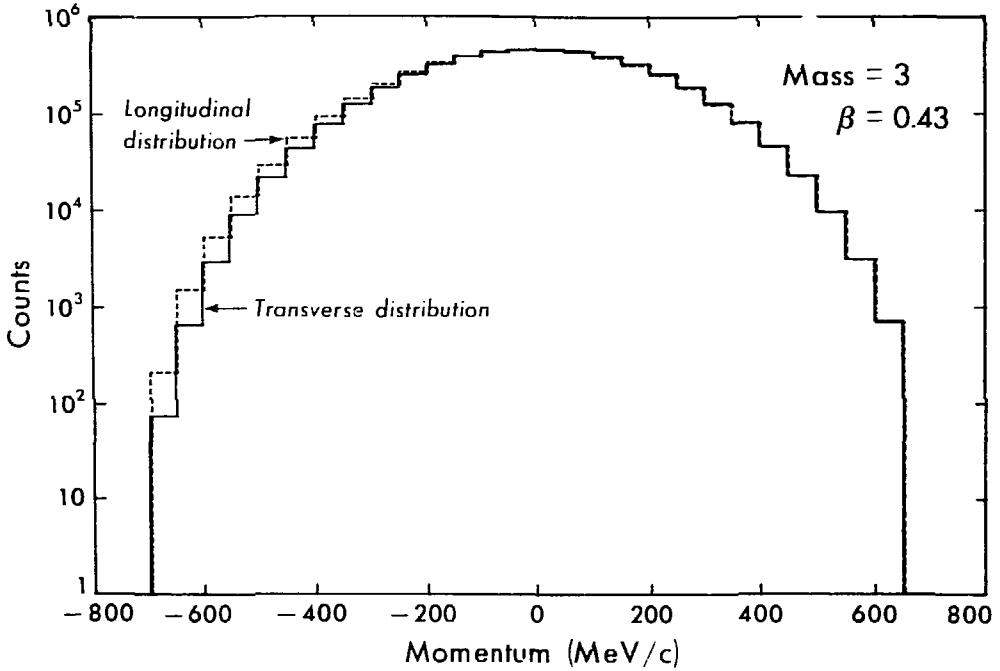

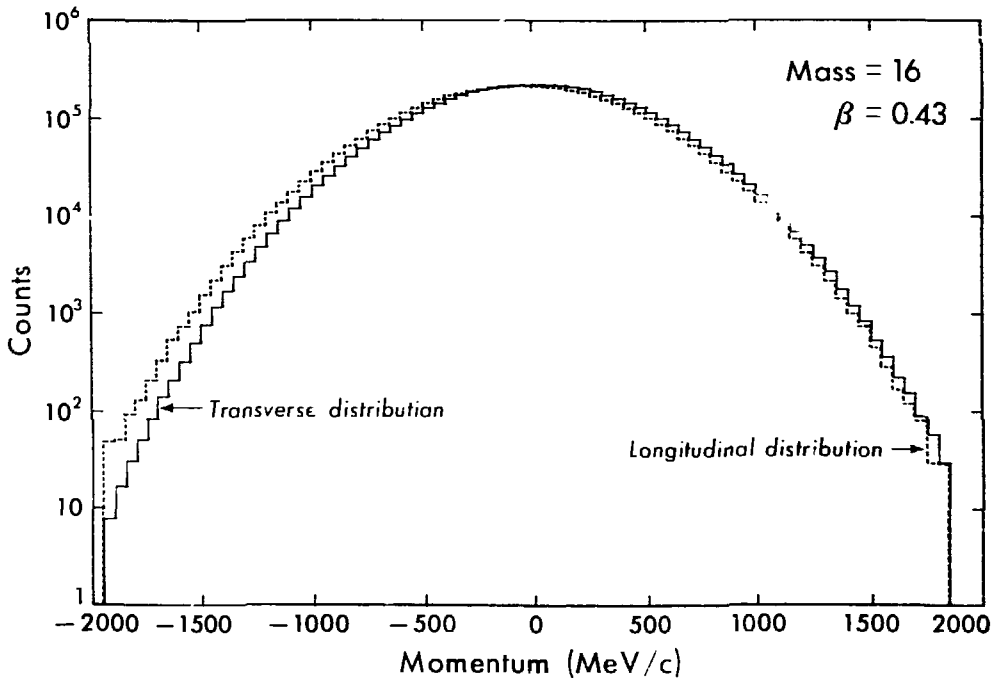

XBL 799-12026

FIGURE 23

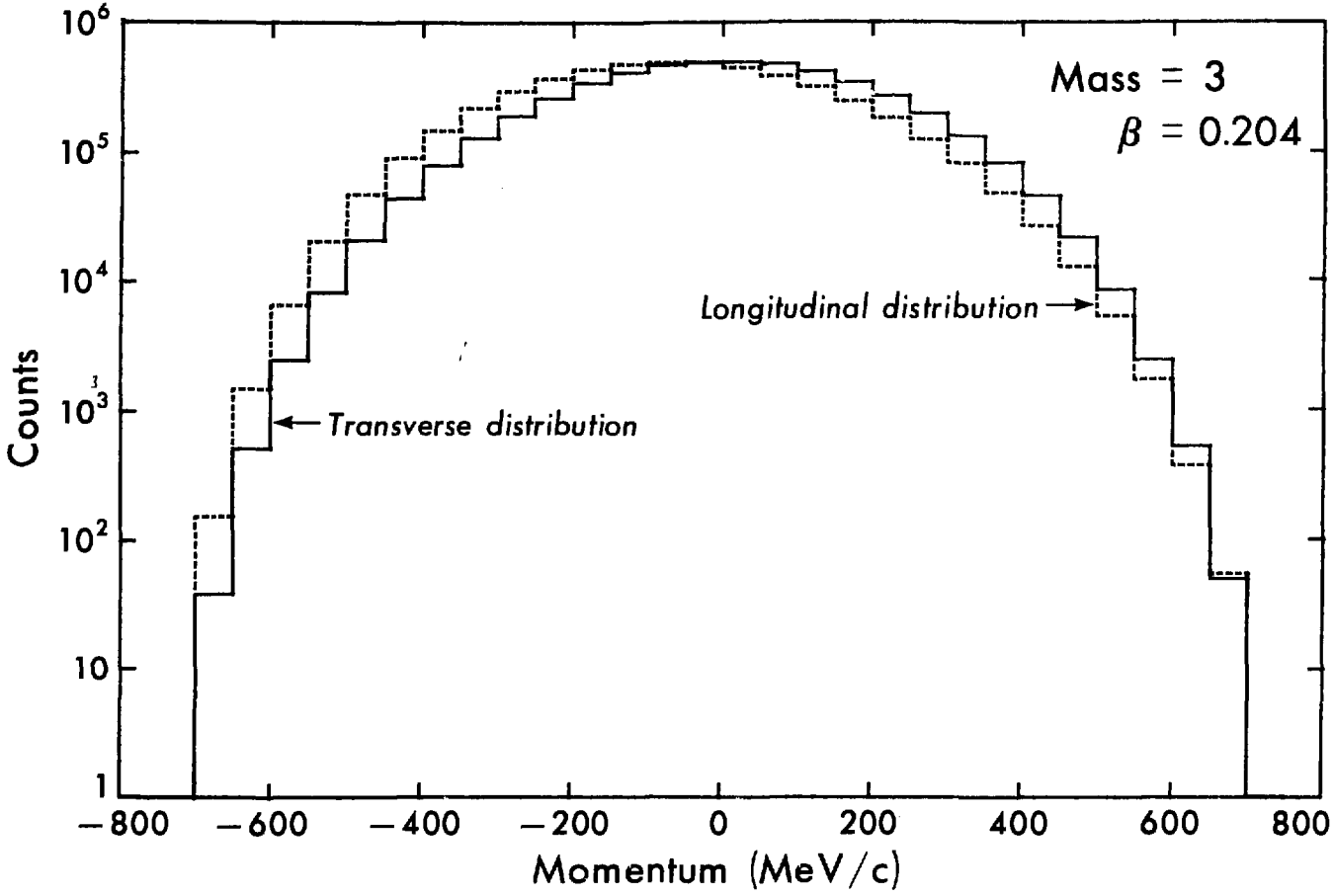

XBL 799-12031

FIGURE 24

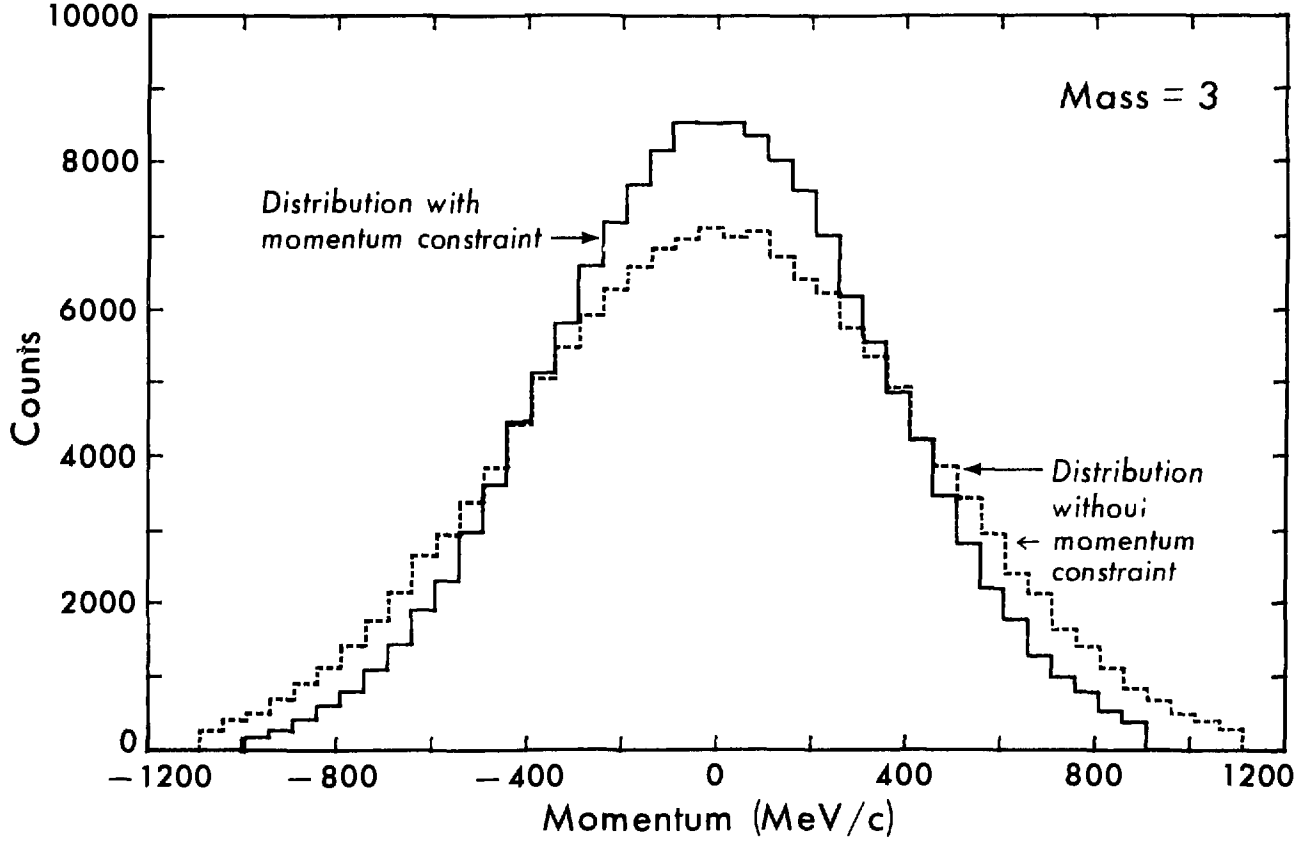

XBL 799-12010

FIGURE 25

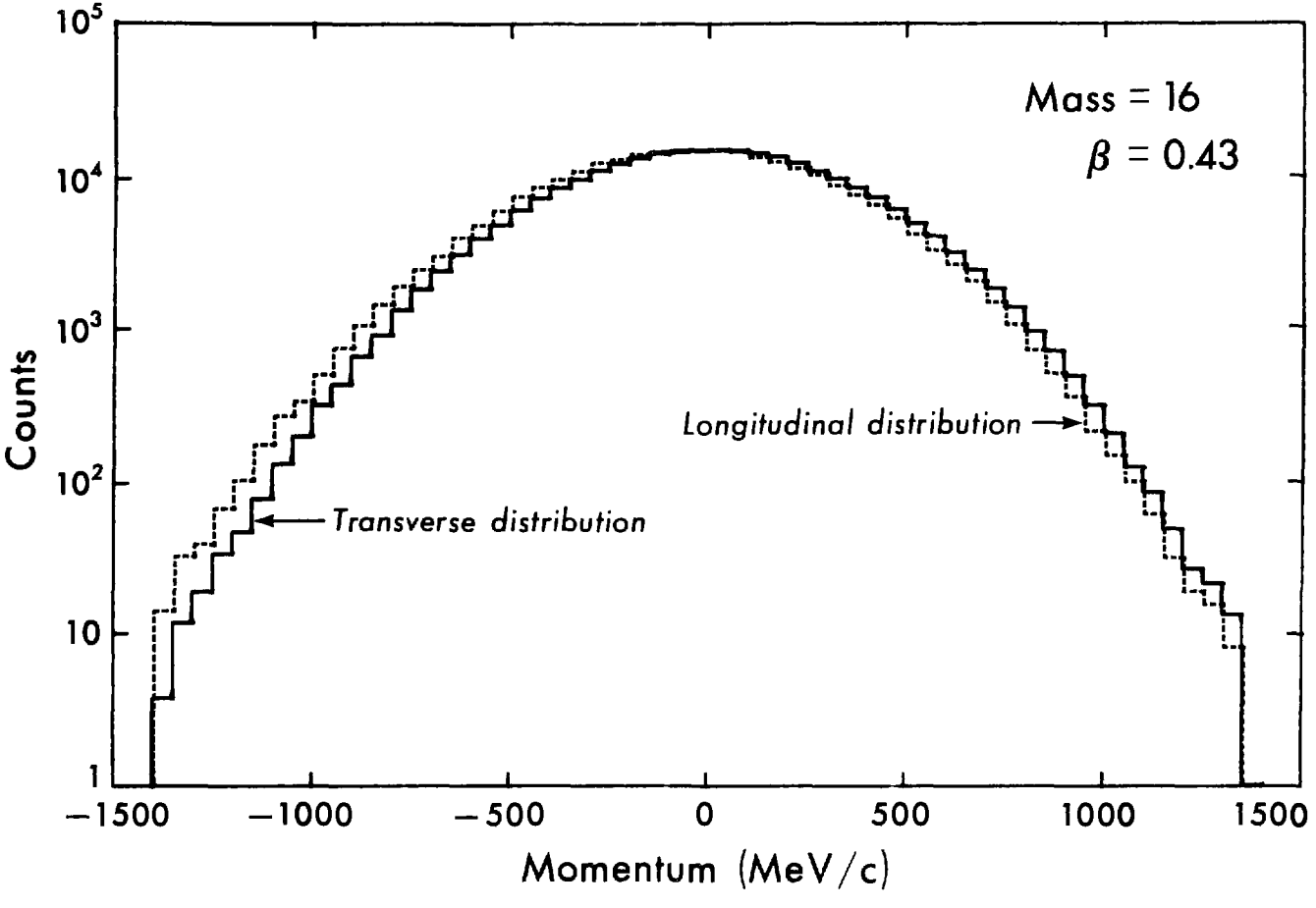

XBL 799-12011

FIGURE 26